DNS STUDY FOR THE ORIGIN OF THE CHAOS IN LATE BOUNDARY LAYER TRANSITION OVER A FLAT PLATE

by

MANOJ KUMAR THAPA

Presented to the Faculty of the Graduate School of

The University of Texas at Arlington in Partial Fulfillment

of the Requirements

for the Degree of

DOCTOR OF PHILOSOPHY

THE UNIVERSITY OF TEXAS AT ARLINGTON

December 2013

To my parents, who are my continuous source of inspiration for consistent hard work, patience and honesty and who made me who I am now.

ACKNOWLEDGEMENTS

I would like to thank my supervising professor Dr. Chaoqun Liu for constantly motivating and encouraging me, and also for his invaluable advice during the course of my doctoral studies. I wish to thank my academic advisors Dr. Benito Chen-Charpentier, Dr. Guojun Liao, Dr. Yue (David) Liu and Dr. Hristo Kojoharov for their interest in my research and for taking time to serve in my dissertation committee.

I would also like to extend my appreciation to Mathematics Department of University of Texas at Arlington for providing financial support for my doctoral studies. I am grateful to Texas Advanced Computing Center (TACC) for providing computation hours.

I am especially grateful to Dr. Ping Liu and Dr. Yonghua Yan for their interest in my research and for the helpful discussions and invaluable comments. I also would like to thank Dr. Shree Krishna Bhattarai for giving time to resolve some technical difficulties of this dissertation. I also thank several of my friends who have helped me throughout my career.

Finally, I would like to express my deep gratitude to my maternal uncle, Tap Bahadur Karki, who shaped my childhood mind and future life. I am also extremely grateful to my beloved wife, Jyoti, for always being on my side. I am extremely fortunate to be so blessed.

November 15, 2013

ABSTRACT

DNS STUDY FOR THE ORIGIN OF THE CHAOS IN LATE BOUNDARY LAYER TRANSITION OVER A FLAT PLATE

MANOJ KUMAR THAPA, Ph.D.

The University of Texas at Arlington, 2013

Supervising Professor: Chaoqun Liu

This dissertation is devoted to the investigation of the origin and mechanism of chaos (asymmetric or disorganized flow) in late boundary layer transition over a flat plate without pressure gradient. This kind of flow not only exists at the very late stage of transition but also is a crucial component for turbulence formation- still not well understood. According to existing theories, the formation of the chaos in late boundary layer transition was considered due to big background disturbances (noises) and use of non-periodic spanwise boundary condition during numerical simulations. It was further assumed that universal coherent structures (ring-like vortices) are first affected by background disturbances, and then the change in the coherent structures quickly affect the small length scale voritces, which directly leads to flow chaos and eventually the laminar flow changes into turbulence. However, after contemplating our high-order Direct Numerical Simulation (DNS) results, we strongly believe that the internal instability of multiple-level ring cycles triggered by overlapping of those cycles is main reason. Further, We observed, a completely new phenomenon, that the flow chaos process begins at middle part of the structure when the third ring cycle overlaps first and second one.

In this work, we also tried trace to as earlier as location for the origination of the chaos atleast for our DNS where certain amplitude of perturbation was introduced only from inlet. A significant asymmetric phenomenon is first noticed from the second cycle at nearly middle of both streamwise and spanwise direction. More technically, a noticeable asymmetric phenomenon in the middle cycle starts at time step $t = 16.25T$ and $x = 838.9\delta_{in}$ where the top and bottom level rings are still completely symmetric. The disorganized (asymmetric) structure of middle level ring quickly affects the small length scale in boundary layer bottom by primary and secondary "sweeps". The disorganized process spreads to top level through multiple level "ejections". In this way, the whole flow domain becomes disorganized in all directions and ultimately the flow state is changed into complex turbulent one. Albeit further research is necessary to complete this work.

TABLE OF CONTENTS

LIST OF ILLUSTRATIONS

LIST OF TABLES

CHAPTER 1

INTRODUCTION

The process of a laminar flow changing into turbulence is known as laminar-turbulence transition. The transitional flow is a fundamental scientific problem of modern fluid dynamics. It has been subject of intensive research for more than a century due to its great importance to various engineering applications in aerospace engineering, mechanical engineering, energy engineering, bio engineering and many others. Our understanding of the problem is still far from complete. Main difficulty in understanding of the problem is it's dependency on the large number of factors which are co-related to each other. However, after hundreds of years of futile efforts to the subject, it is known that the process completes through a series of stages [1, 2, 3]. This is an extraordinarily complicated process-One of the most challenging still fascinating unsolved problems of natural science-from antiquity to present days.

Although the laminar-turbulent transitional process applies to all kind of fluid flows, it is most often related to the context of boundary layers and in fact most of laminar-turbulence researches are concentrated on the transition related with boundary-layers. The boundary-layers are ubiquitous in all kinds of real flows and their important role in a variety of practical applications. For instance, delaying the onset of transition phenomenon on an airfoil definitely reduces the frictional force (drag), hence decreasing the fuel consumption of the aircraft [4]. However, for the optimized flow control demands the fundamental understanding of the transitional flow in boundary layer.

The following comments about the turbulence can be found in Wikipedia web page at http://en.wikipedia.org/wiki/Turbulence, made by some great Scientists. Nobel Laureate

Richard Feymann described turbulence as "the most important unsolved problem of classical physics." According to an apocryphal story, another Nobel Laureate Werner Heisenberg was asked what he would ask God, given the opportunity. His reply was: "When I meet God, I am going to ask him two questions: Why relativity? And why turbulence? I really believe he will have an answer for the first." A similar witticism has been attributed to Horace Lamb . Lamb was quoted as saying in a speech to the British Association for the Advancement of Science, "I am an old man now, and when I die and go to heaven there are two matters on which I hope for enlightenment. One is quantum electrodynamics, and the other is the turbulent motion of fluids. And about the former I am rather optimistic." Note that they weren't very optimistic for the turbulence. Actually, the mechanism of turbulence formation is still a veil of mystery in the nature.

Turbulence-one of the top secrets of the nature, in general, is composed of two main parts: small length-scale vortices generation and chaos formation [5, 6]. Despite the great amount of research devoted to the mechanism of turbulence formation and sustenance in late boundary layer transition , there are only very few research papers about the mechanism of chaotic flow in late boundary layer transition [7, 8, 9, 10] . One main reason may be that fluid dynamic community always relied on the classical theories (main classical theories are presented in section 1.1) at least for turbulence generation and sustenance. According to the classical theories, turbulence is generated when the large vortices at very late stage of boundary-layer transition breakdown into smaller vortices. The vortices again breakdown into further smaller pieces. Finally , small length length-scales will be formed. The energy will be distributed throughout division. Unfortunately, breakdown and re-connection process couldn't be observed by our DNS. Moreover, this phenomenon is theoretically impossible and could never happen in practice [11].

While taking into an account of earlier research works about the mechanism of chaos formation at late boundary layer transition, one milestone work was done by Daniel Meyer

and his colleagues [7]. They believed that "the inclined high-shear layer between the legs of the vortex exhibits increasing phase jitter (i.e. chaos) starting from its tip towards the wall region." However, from our numerical simulation, we observed a phenomenon which is different from the theory given by Meyer and his co-workers. We use periodic boundary condition in span-wise direction and disturbances are present only at inflow, outflow and far field. Still, we observe chaotic flow. So, it is unlikely to consider flow chaos due to back ground noise and use of non-periodic condition in spanwise direction.

In general, turbulence or turbulent flow is characterized by chaotic and seemingly random property changes in time and space co-ordinates. More, it is highly irregular(sensitive to initial conditions),has efficient mixing capability (rapid diffusion of mass, momentum and energy) and contains vorticity components [12, 13]. Then obviously some of fundamentally important questions may come to our mind such as from where irregular fluctuation starts and by which mechanism flow becomes chaotic?

In order to get deep understanding on the nature of the nonlinear stages of late flow transition in a boundary layer, we recently conducted a high order direct numerical simulation (DNS) over a flat plate without an adverse pressure gradient at Mach number 0.5 based on the complete solution of Navier-Stokes equations governing fluid motion with $1920 \times 128 \times 241$ grid points and about 600,0000 time steps. Based on the DNS results, our research group has investigated many significant role playing phenomena in the late stages of the transition - nonlinear growth of disturbances, evolution of universal coherent structures, multiple rings formation, small length scales generation, transfer of energy from inviscid region to the boundary layer wall turbulence etc.- and purposed a novel approach about turbulence generation and sustenance in late boundary layer transition [14, 15].

It is interesting to note that most of researches in this area are either on very earlier stages of evolution (typically on linear stage and weakly nonlinear stage) or after the flow is well developed (mostly after well developed turbulent flow). Due to the mysterious nature

of turbulence, researchers are trying to attack the subject matter with different approaches such as, some groups assume that the coherent vortical structures play significant role, while other downplay the importance of such structures and advocate the use of purely statistical methods [9].

In this work, we concentrate our investigation mainly at the last and very complex stage of transition process-the origination and formation of chaos. The chaos is an important constituent of turbulence.It is well validated since the age of Reynolds that the first appearance of the turbulence is very sensitive to the size of the disturbances at the inlet and the type of inlet. We thoroughly investigate our well validated DNS results and try to trace as earliest as possible location and time step for fixed size of disturbances introduced in inlet only (validation will be presented in chapter 2). We also try to shed some more light on the mechanism about chaos formation in late boundary layer transition. It has been found an interesting directly propositional relation between skin-friction drag and small scale vortices genration near the wall. The mechanism of boundary layer thickening is also investigated which will be explained in chapter 5.

1.1 Classical theories on turbulence generation and sustenance

1.1.1 Richardson's vortex and energy cascade theory (1928)

Being impressed from Jonathan Swift's poem (left side of Figure 1.1), Richardson assumed that a turbulent flow is composed by "eddies" of different length scale. The large eddies will be stretching, unstable and breaking up to smaller eddies. These smaller eddies undergo the same process, giving rise to even smaller eddies which produces a hierarchy of eddies. This process will continue until reaching a sufficiently small length scale such that the viscosity of the fluid can effectively dissipate the kinetic energy into internal energy.The energy cascades from these large-scale eddies to smaller scale eddies by an inertial and

essentially inviscid mechanism and the kinetic energy of the initial large eddy is divided into the smaller eddies [16].

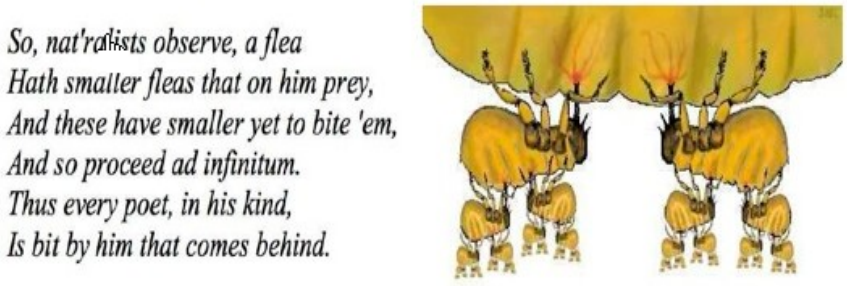

Figure 1.1: A schematic representation of Richardson's energy cascade process (Frisch et al, 1978).

1.1.2 Kolmogorov assumption (1941)

In 1941, Andrey Kolmogorov, a famous russian mathematician introduced the classical theory on turbulence [17, 18]. In general, large length-scales of a flow are not isotropic, because they are determined by the characteristic length of the apparatus. For example, the largest integral length scale of pipe flow is equal to the pipe diameter. Agreeing with Richardson, Kolmogorov postulated that in the Richardson's notion of energy cascade, the geometrical and directional information is lost, while the scale is reduced and so that the statistics of the small scales has a universal character. Means when the Reynolds number is sufficiently high, the smallest length scales are statistically isotropic for all turbulent flows. Actually, it was assumed that there is no dissipation during the energy transfer from large vortex to small vortex through "vortex breakdown".

1.1.3 Kolmogorov's first and second hypotheses (1941)

Based on his assumption, Kolmogorov (1941) further gave two very famous theories on smallest length scale, which is later called Kolmogorov scale (first hypothesis), and turbulence energy spectrum (second hypothesis) [19]:

$$\eta = (\frac{\nu^3}{\epsilon})^{\frac{1}{4}},$$

$$E(k) = C\epsilon^{\frac{2}{3}}\kappa^{-\frac{5}{3}} \; and$$

$$\epsilon = \gamma\{2(\overline{\frac{\partial u_1}{\partial x_1}})^2 + 2(\overline{\frac{\partial u_2}{\partial x_2}})^2 + 2(\overline{\frac{\partial u_3}{\partial x_3}})^2 + (\overline{\frac{\partial u_2}{\partial x_1} + \frac{\partial u_1}{\partial x_2}})^2 + (\overline{\frac{\partial u_3}{\partial x_2} + \frac{\partial u_2}{\partial x_3}})^2 + (\overline{\frac{\partial u_1}{\partial x_3} + \frac{\partial u_3}{\partial x_1}})^2\}$$

where, η is Kolmogorov scale, ν is kinematic viscosity, ϵ is the rate of turbulence dissipation, E is the energy spectrum function, C is a constant and κ is the wave number. These formulas were obtained by Kolmogorov's hypothesis that the small length scales are determined by ν and ϵ, and E is related to κ and ϵ.

1.2 A brief review of researches on the laminar-turbulence transition

The word " turbulence" comes from the Latin word: turbulentia, which originally refers to the disorderly or irregular motion of a crowd (turba).In the middle age the word turbulence was frequently used to indicate just "trouble". Even today the word may refer to social and personal behavior. Scientifically there is no accurate definition of the turbulence covering every aspect of it but it can be characterized by some important features such as disorderly motion, with high mixing scale and presence of vorticity components. These characteristics are very helpful to distinguish the turbulent flow from other various wave-like flows from our nature [10].

The turbulent flow has attracted human being since long time ago. More than two thousand years ago Lucretius explains about eddy motion in his book "De rerum natura" [20]. Over five centuries ago Leonardo da Vinci was probably the first to originated the

word the turbulence (in Italian turbolenza) with its scientific meaning and to observe the various sizes of eddies formed behind the pillars of a bridge Figure (1.2).

Figure 1.2: Leonardo's imagery of falling water (1508-1509).

Nearly after a century later, Euler (1757) introduced the rigorous mathematical equations of incompressible or inviscid (zero-viscosity) flow in both two and three dimensions and realized the importance of vorticity. Seventy years later Navier (1827) generalized these equation to include viscosity. Because of further work by Stokes (1845), the equations are known as the NavierStokes equation. They constitute a set of nonlinear and nonlocal evolution equations for the three-dimensional velocity field. Kelvin was the first to propose studying turbulence using random solution of the Navier-Stokes equations. In 1883, Osborne Reynolds was first to make an early hypothesis on the mechanism of laminar-

turbulence transition by conducting various pipe flow experiments (Reynold's dye experiment). He assumed that transition is consequence of instability of the laminar boundary layer. Further, he introduced a dimensionless number (now called the Reynolds number) $Re = \frac{LV}{\gamma}$, where L and V are a typical length scale and a typical velocity of the flow. Laminar, transitional (intermittently turbulent) and fully developed turbulent pipe flow were illustrated by experiments as shown Figure 1.3. A lot more information on the early history of the subject can be found on the book [21].

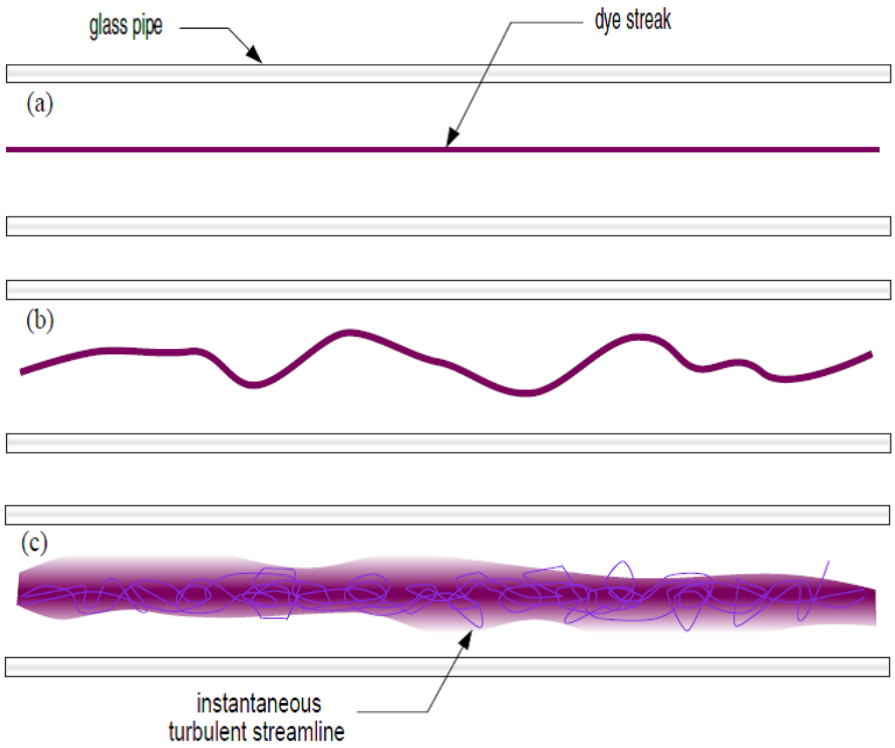

Figure 1.3: The Reynolds experiment; (a) Laminar flow, (b) Transitional flow (still laminar) ,and (c) Turbulenence [G. Degrez,2012].

One of the major breakthrough on the research of transition from laminar to turbulent flow, which expedited whole theoretical and experimental research into a great height, was Luding Prandtl's (1904) boundary-layer concept. The notion that in flows over solids

at high Reynolds numbers, the effects of viscosity are important only in a thin layer in the vicinity of the solid boundary. From that point of time, the general laminar-turbulent flow research was/is shifted to boundary-layer transition. Heisenberg (1924) investigated linear hydro-dynamic stability theory for laminar flow and nature of turbulence by using the OrrSommerfeld equation, a fourth order linear differential equation for small disturbances from laminar flow. The first calculation of boundary layer stability were achieved by the pioneer works of Tollmien (1928) [22] and Schlichting (1933) [23, 24]. Schubauer & Skramstad (1948) [25], Liepmann (1943) [26], Laufer and Vrebalovich (1960) [27] and Kendall (1967) [28] demonstrated important role of small-disturbance stability theory providing a basis for Reynolds-Rayleigh hypothesis for the mechanism of transition. Now it is well established that the transition to turbulence in shear flows at small and moderate levels of environmental disturbances occurs through development of instability waves in the laminar base flow. During the period of $1930 - 1970$ the concept of boundary-layer transition was widely enlarged mathematically and experimentally [29].

Nevertheless, some researchers have tried to study the transition mechanism independently of stability theory. These efforts have produced neither a reliable transition mechanism nor any clue of predicting transition Reynolds numbers [30].

The physical mechanism of boundary-layer transition greatly depend upon the nature of base flow, amplitude of environmental disturbances and surface roughness [2] . Based on the growth of perturbation in the boundary-layer, there are mainly two classes of transition are known [31, 32, 33, 34]. The first type of scenario is known as "natural" transition. It is one of the more common methods by which a laminar boundary layer transitions to turbulence. The T-S waves are initiated with the transformation of environmental disturbances into perturbations when some disturbance (sound, for example) interacts with leading edge roughness in a process known as receptivity. These waves are slowly amplified as they move downstream until they may eventually grow large enough that nonlinearities take

over and the flow transitions to turbulence. This kind of transition takes place only when environmental disturbances have relatively weak intensity. The second type of transition is referred as "bypass" transition which is associated with the extremely high level of perturbations where the laminar flow directly changes into turbulent flow.

As we are concerned for purely fundamental mechanism of the transition, we put our effort on first type of transition (natural transition). Actually, most of laminar-turbulence transition researches are carried out for the natural transition.

The transition process in boundary-layer complete through a complicated sequences of spatial changes. The initial phase of the natural transition process is referred as the receptivity [32, 35] where the transformation of environmental disturbances (both acoustic and vortical) into small instability modes occur within the boundary-layer. In general, it has been well believed that acoustic disturbances are responsible for the growth of two-dimensional instabilities such as Tollmien-Schlichting waves (T-S waves), while vortical disturbances are responsible to the growth of three-dimensional phenomena such as the cross-flow instability [3].

Initially these instability modes may be small enough so can't be measure,their presence can only be realized only after the onset of an instability. In this case, the initial amplification (growth or decay) of environmentally-generated wave can be well predicted by the linear instability theory [36]. If these amplitude attain maximum value (1-2 % of free-stream velocity) [2] then the flow enters into a different phase-as the instability modes grow and distort the mean flow and linear stability theory no longer applies. The non-linear development such as large coherent structure, small length scale generation, disorderly flow formation takes place in this phase. The earlier stage of the non-linear phase is also known as weakly non-linear.

At late (essentially nonlinear) stages the two types of transition are characterized by transformation of instability waves into intensive vortical structures. λ-vortices are the

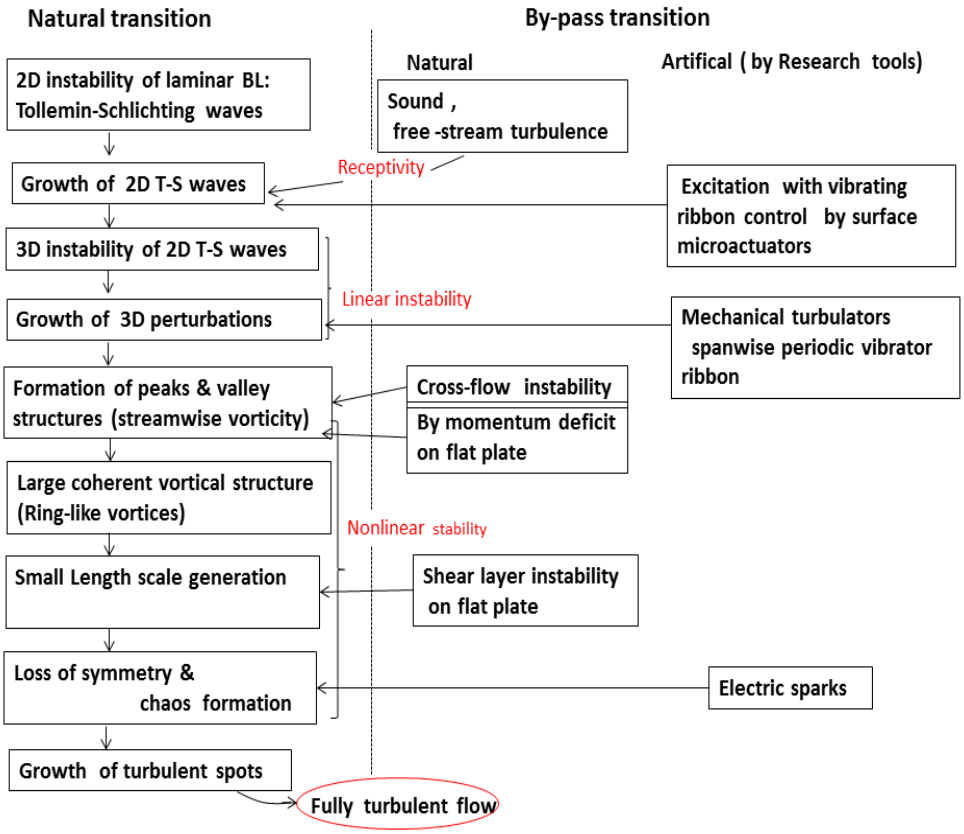

Figure 1.4: Schematic of boundary-layer transition.

most typical of them [37]. They start to form at weakly nonlinear stages and have different peculiar properties and relative spatial positions in the K-type (alligned) [38] and N-type (staggered) [31]. However, it has been found in later experiments [39, 40]that local nonlinear mechanisms of boundary-layer break-down observed in the in both regions in the vicinity of Λ-vortices are qualitatively same.This similarity was fond also in case of a pulse-like excitation when only single Λ-structure was formed in the boundary-layer at nonlinear stage of transition development [41]. These results have shown that the mechanisms of disturbance development predominant at late stages of of boundary-layer transition are rather universal: First a Λ-vortex is generated, then the Λ-vortex becomes the hairpin and ring-like vortex,and a chain of ring-like vortices are developed.

Although the enormous amount of research is devoted on the subject matter, the level of understanding of each phase varies greatly, from near complete understanding of primary mode growth to little knowledge about late stages of transition. After over a hundred of years of futile study , there has been a significant progress for understanding linear and weakly non-linear stages of flow transition [2, 31]. However, for late non-linear transition stages, there are still many questions remaining for research [42, 43, 44, 45, 46, 47]. Adrian (2007) [48] generated hairpin vortex organization in wall turbulence, but we can't find any discussion about the important constitute such as the 'sweep' and 'ejection' events and the possible playing of the shear layer instability. Wu & Moin (2009) [49] claimed a new DNS for flow transition on a flat plate. They did obtained fully developed turbulent flow with ring-like vortices structure by flow transition at zero pressure gradient. Still, they did not discuss about the important mechanism of boundary layer transition such as sweeps, ejections, positive spikes exctra. Recently, Guo et al(2010) [50] conducted an experimental study for late boundary layer transition with . They believed that the U-shaped vortex is a barrel-shaped head wave, secondary vortex, and is induced by second sweeps and positive spikes.

1.3 Questions to classical theory on boundary-layer transition

The classical theory considers "vortex breakdown" as the last stage of boundary layer transition on a flat plate. According to Richardson's energy cascade and Komogorovs assumption, "vortex breakdown" is a unique source of turbulence generation. The serious weakness of classical theory given by Richardson and Kolmogorov is that nobody ever observed the "vortex breakdown" process. While Komogorovs third hypothesis or $(-\frac{5}{3})$ spectrum law is proved correct, Richardsons eddy cascade and vortex breakdown, Kolmogorov first (statistically isotropic for small eddies) and second (Kolmogorov scales) hypotheses

are never confirmed. As a roughly estimation, 15 vortex breakdown cycles are needed to get Kolmogorov scale for a Reynolds number of 10^5 , but even a single vortex breakdown has not been observed yet. As the experiment tools are so powerful and the visualization technology is so advanced nowadays, it is very hard to believe one still cannot detect the vortex breakdown process. **The only conclusion we can believe is that the classical theory on turbulence generation may need to be revisited** . Although the classical turbulence theory is about the high Reynolds number flow and the topic discussed here is mainly the transitional flow, it is not believed there are two different mechanisms for turbulence generation.

Dr. Chaoqun Liu presented a new theory on turbulence generation and sustenance recently [11, 14]. The new theory is able to well interpret the physics of turbulence which is currently considered by many people as a topic "impossible to understand, impossible for ever, or God has no answer." Contradicting to most of classical theory and/or currently dominant theories, Liu's theory may bring a revolution to not only the basic fluid mechanics, but also to flow control for flow transition, turbulence, drag reduction, design optimization, etc. It may also bring a revolution to turbulence modeling.

1.4 New theory on boundary layer transition by Liu

Classical theory on boundary layer transition can be described by four stages: 1) Boundary layer receptivity; 2) Linear instability; 3) Non-linear growth; 4) Vortex breakdown to turbulence. Apparently, we disagree with the classical theory on "vortex breakdown to turbulence". The new theory of boundary layer transition can be described by five stages: 1) Boundary layer receptivity; 2) Linear instability; 3) Large vortex structure formation; 4) Small vortices generation; 5) Symmetry loss and "chaos formation". By the

way, the vortex cascade in turbulence given by Richardson, Kolmogorov and others is not observed.

1.5 Summary of the new theory on turbulence generation by Liu

The new theory on turbulence formation and sustenance shows that all small length scales (turbulence) are generated by shear layer instability which is produced by large vortex structure with multiple level vortex rings, multiple level sweeps and ejections, and multiple level negative and positive spikes near the laminar sub-layers. Therefore, "turbulence" is not generated by "vortex breakdown" but rather positive and negative spikes and consequent high shear layers. "Shear layer instability" is considered as the "mother of turbulence". This new theory may give a universal mechanism for turbulence generation and sustenance - the energy is brought by large vortex structure through multiple level sweeps.

1.6 Highlights of Liu's turbulence theory

1. The fluid motion can be mainly decomposed as a pure shear part and rotation part ignoring the translation part. The shear part is conditionally unstable and rotational part is stable. The laminar flow is dominated by shear part and the turbulent flow is dominated by rotation. Flow has trend to change the shear part to rotation when away from the wall. Therefore, flow transition from laminar state (unstable) to turbulent flow (stable) is doomed.
2. The vorticty is large near the wall surface where the shear is dominant. The role of all linear unstable modes is to push the vorticity up from the wall (roll up). The flow trend to change shear to rotation will occur inside the flow field and the spanwise vortex will form due to the trend from shear to rotation. The unstable linear modes

are small and cannot form vortex. Therefore, the N-factor which is based on linear analysis is questionable.

3. The linear unstable modes cannot form vortex and the non-linear stage is not interaction of 2-D modes with 3-D modes, but spanwise vortex with 3-D modes. The analytic linear solution departs from DNS at the beginning. They do not agree with each other even in very early stages.
4. There is no such a process that the Λ-vortex self deforms to hairpin vortex. The Λ-vortex root and ring head are formed separately and ring is not part of Λ-vortex.
5. Λ-vortex is a pair of open rotation cores (never close) and is not a vortex tube
6. A momentum deficit zone (low speed zone) is formed above the Λ-vortex and further generates a Λ shaped high shear due to the vortex root ejection. The vortex rings are generated by the high shear layer (K-H type) instability
7. Multiple vortex rings are all formed by shear layer instability which is generated by momentum deficit (There are not vortex breakdown and reconnection and multiple ring formation is not governed by Crow theory)
8. U-shaped vortex is a tertiary vortex with the same sign of vorticity as the prime vortex
9. The vortex structure is stable and can travel for long distance. "Votex breakdown" never happened and is theoretically incorrect
10. No matter how to define "vortex", small vortices (turbulence) cannot be generated by "vortex breakdown". All small vortices are generated by shear layer without exception. In other words, "shear layer instability is the mother of turbulence"
11. If we define vortex is a rotation core, the rotation core is stable and cannot breakdown. Therefore "vortex breakdown" cannot happen. The only way is that the vortex can be weakened by dissipation when it travels.
12. The multiple level shear layers are generated by vortex sweeps and ejections. The sweep brings high speed flow down (positive spike) to the lower boundary layer and

the ejection brings the low speed flow up (negative spike) to the upper boundary layer. They form the multiple level shear layers

13. These multiple shear layers generate small vortices with different sizes
14. The energy transport channel is that the high energy is brought down to the lower boundary layer by multiple level sweeps. Without these sweeps, all small vortices (turbulence) would dissipate quickly
15. Large vortex cannot pass energy to smaller vortices through "vortex breakdown" which was never observed by any experiment or DNS
16. The disordering of flow structure is mainly not caused by the background noise or non-symmetric spanwise boundary condition, but internal property of the vortex structure. The non-symmetry starts in the middle of the vortex package. The classical theory including the Richardson's eddy cascade, Kolmogorov universal and isotropic hypothesis on smallest vortices, Kolmogorov small length scales are not confirmed and observed. Their theory should be revisited.
17. Richardson eddy cascade revisit **(There is no such a cascade)**
18. Kolmogorov hypothesis revisit **(There is no vortex breakdown and there is no energy passing through vortex breakdown. There is no proof of existence of Kolmogorov small scale.)** The smallest scale should be determined by smallest shear layer which is measured by $y^+(1-10)$
19. There is no "turbulence intermittence". The faked term is generated by misunderstanding of turbulence package self motion and relative motion
20. There is no "vortex breakdown" which is caused by faked visualization by using improper λ_2 values.

CHAPTER 2

CASE SET UP AND CODE VALIDATION

2.1 Governing equations

The Navier-Stokes equations governing the flow of viscous compressible ideal gas in vector form are

$$\rho[\frac{\partial q}{\partial t} + (q.\nabla)q] = \nabla p + \nabla.[\lambda(q.\nabla)\bar{\bar{I}}] + \nabla.[\mu(\nabla q + \nabla q^{tr})] \tag{2.1}$$

$$\frac{\partial q}{\partial t} + \nabla.(pq) = 0 \tag{2.2}$$

$$\rho c_p[\frac{\partial h}{\partial t} + (q.\nabla)h] = \nabla.(k\nabla h) + \frac{\partial p}{\partial t} + (q.\nabla)p + \Phi \tag{2.3}$$

$$p = \rho RT \tag{2.4}$$

where, $q = (u, v, w)$ is the velocity vector, ρ the density, p the pressure, τ is the temperature, R the ideal gas constant, c_p the specific heat at constant pressure, k the thermal conductivity, μ the first coefficient of viscosity, λ the second coefficient of viscosity. The viscous dissipation Φ is given by $\Phi = \lambda(q.\nabla)^2 + \frac{\mu}{2}[(\nabla q + \nabla q^{tr})]^2$.

The three-dimensional governing Navier-Stokes equations for a compressible fluid can be derived into generalized curvilinear coordinates in a conservative form as follows [51]:

$$\frac{1}{J}\frac{\partial Q}{\partial t} + \frac{\partial(E - E_v)}{\partial \xi} + \frac{\partial(F - F_v)}{\partial \eta} + \frac{\partial(H - H_v)}{\partial \zeta} = 0 \tag{2.5}$$

Where, the vector of conserved quantities Q, inviscid flux vector (E, F, G), and viscous flux vector (E_v, F_v, G_v) are defined as follows :

$$Q = \begin{bmatrix} \rho \\ \rho u \\ \rho v \\ \rho w \\ e \end{bmatrix}, \; E = \frac{1}{J} \begin{bmatrix} \rho U \\ \rho u U + p\xi_x \\ \rho v U + p\xi_y \\ \rho w U + p\xi_z \\ U(e+p) \end{bmatrix}, \; F = \frac{1}{J} \begin{bmatrix} \rho V \\ \rho u V + p\eta_x \\ \rho v V + p\eta_y \\ \rho w V + p\eta_z \\ V(e+p) \end{bmatrix},$$

$$H = \frac{1}{J} \begin{bmatrix} \rho W \\ \rho u W + p\zeta_x \\ \rho v V + p\zeta_y \\ \rho w V + p\zeta_z \\ W(e+p) \end{bmatrix}, \; E_v = \frac{1}{J} \begin{bmatrix} 0 \\ \tau_{xx}\xi_x + \tau_{yx}\xi_y + \tau_{zx}\xi_z \\ \tau_{xy}\xi_x + \tau_{yy}\xi_y + \tau_{zy}\xi_z \\ \tau_{xz}\xi_x + \tau_{yz}\xi_y + \tau_{zz}\xi_z \\ q_x\xi_x + q_x\xi_y + q_z\xi_z \end{bmatrix},$$

$$F_v = \frac{1}{J} \begin{bmatrix} 0 \\ \tau_{xx}\eta_x + \tau_{yx}\eta_y + \tau_{zx}\eta_z \\ \tau_{xy}\eta_x + \tau_{yy}\eta_y + \tau_{zy}\eta_z \\ \tau_{xz}\eta_x + \tau_{yz}\eta_y + \tau_{zz}\eta_z \\ q_x\eta_x + q_x\eta_y + q_z\eta_z \end{bmatrix}, \; H_v = \frac{1}{J} \begin{bmatrix} 0 \\ \tau_{xx}\zeta_x + \tau_{yx}\zeta_y + \tau_{zx}\zeta_z \\ \tau_{xy}\zeta_x + \tau_{yy}\zeta_y + \tau_{zy}\zeta_z \\ \tau_{xz}\zeta_x + \tau_{yz}\zeta_y + \tau_{zz}\zeta_z \\ q_x\zeta_x + q_x\zeta_y + q_z\zeta_z \end{bmatrix}$$

More, $J = \frac{\partial(\xi,\eta,\zeta)}{\partial(x,y,z)}$ is the jacobian of coordinate transformation between the Curvilinear (ξ, η, ζ) and Cartesian (x,y,z) frames, and ξ_x,ξ_y, ξ_z,η_x, η_y, η_z,ζ_x, ζ_y, ζ_z are coordinate transformation matrices. The contravariant velocity components U,V,W are defined as follows [52, 53, 54]:

$$U = u\xi_x + v\xi_y + w\xi_z,$$

$$V = u\eta_x + v\eta_y + w\eta_z,$$

$$W = u\zeta_x + v\zeta_y + w\zeta_z$$

where, e is the total energy. The components of viscous stress and heat flux are denoted by τ_{xx}, τ_{yy}, τ_{zz}, τ_{xy},τ_{xz}, τ_{yz} and q_x, q_y, q_z respectively.

We change Equation (2.5) into dimensionless form by using the following reference values for length, density, veloities, temperature, pressure and time as L, ρ_∞, U_∞, T_∞, p_∞ and $\rho_\infty U_\infty^2$ respectively. The Reynolds number and the Mach number are defined as
$Re = \frac{\rho_\infty U_\infty \delta_{in}}{\mu_\infty}$,
$M_\infty = \frac{U_\infty}{\sqrt{\gamma R T_\infty}}$ respectively and the Prandtl number is defined as
$Pr = \frac{C_p \mu_\infty}{k_\infty}$, here μ_∞ is the viscosity, δ_{in} is the displacement thickness. The specific heat coefficients at constant pressure c_p and the specific heat coefficient at constant volume c_v are related by
$c_p = \gamma c_v$ and $c_p - c_v = R$ and $c_v = \frac{R}{\gamma - 1}$.
In this work, Pr=0.7 and $\gamma = 1.4$. Sutherland's formula in dimensionless form is used to determine the viscosity as:
$\mu = \frac{T^{3/2}(1+S)}{T+S}$, $S = \frac{110.3K}{T_\infty}$.

Equation (2.5) is written as :

$$\frac{\partial Q}{\partial t} = R \tag{2.6}$$

Where the right hand side of the Equation (2.6), R, is given by

$$R = -J[D_\xi(E - E_v) + D_\eta(F - F_v) + D_\zeta(G - G_v)] \tag{2.7}$$

The symbols D_ξ,D_η,D_ζ represent the partial differential operators in the ξ,η and ζ directions respectively.

2.2 Numerical methods

A regular central difference scheme where five points are used to get fourth order numerical error is given as:

$$f_j^{'} = \frac{f_{j-2} - 8f_{j-1} + 8f_{j+1} - f_{j+2}}{12h} + O(h^4)$$

A Sixth Order Compact Scheme (five points and two derivatives to get sixth order) :

$$\frac{1}{3}f_{j-1}^{'} + \frac{1}{3}f_{j+1}^{'} = \frac{1}{h}(-\frac{1}{36}f_{j-2} - \frac{7}{9}f_{j-1} + \frac{7}{9}f_{j+1} + \frac{1}{36}f_{j+2}) + O(h^6)$$

The right side of the Equation (2.6) is discretized by using a six order finite difference compact scheme developed by S. Lele [55] for the spatial discretization in stremwise direction and wall normal directions. For internal points $j = 3, ..., N-2$, the the six order compact scheme is as follows:

$$\frac{1}{3}f_{j-1}^{'} + \frac{1}{3}f_{j+1}^{'} = \frac{1}{h}(-\frac{1}{36}f_{j-2} - \frac{7}{9}f_{j-1} + \frac{7}{9}f_{j+1} + \frac{1}{36}f_{j+2}), \tag{2.8}$$

where, $f^{'}$ is the derivative at point j.

The fourth order compact scheme is used at points j= 2,N-1, and the third order one-sided compact scheme is used at the boundary points j=1,N.

In the spanwise direction where periodic conditions are applied, the pseudo-spectral method is used. In order to eliminate the spurious numerical oscillations caused by center difference schemes, a high-order spatial scheme is used instead of artificial dissipation. An implicit sixth-order compact scheme [55] for space filtering is applied for primitive variables u, v, w, ρ, p after a specified number of time steps. The high-order implicit filter given as:

$$\alpha\hat{\phi_{i-1}} + \hat{\phi}_i + \alpha\phi_{i-1} = \sum_{n=0}^{N} \frac{a_n}{2}(\phi_{i+n} + \phi_{i-n})$$

where $2N$ is the number of neighboring points, $\hat{\phi}$ is filtered and ϕ is the original.

The left side of the Equation (2.6) is time integrated explicitly by a 3rd order TVD Runge-Kutta scheme [56];

$$
\begin{aligned}
&Q^0 = Q^n \\
&Q^1 = Q^0 + \Delta t R^0 \\
&Q^2 = \frac{3}{4}Q^0 + \frac{1}{4}Q^1 + \frac{1}{4}\Delta t R^1 \\
&Q^{n+1} = \frac{1}{3}Q^0 + \frac{2}{3}Q^2 + \frac{2}{3}\Delta t R^2
\end{aligned}
\tag{2.9}
$$

CFL ≤ 1 is required to ensure the stability.

The adiabatic and the non-slipping conditions are enforced at the wall boundary on the flat plate. On the far field and the outflow boundaries, the non-reflecting boundary conditions [56, 57] are applied. Based on the 1-D characteristic analysis, the hyperbolic terms in the ξ direction can be modified as:

$$
\begin{aligned}
&\frac{\partial \rho}{\partial t} + d_1 + V\frac{\partial \rho}{\partial \eta} + \rho(\eta_x\frac{\partial u}{\partial \eta} + \eta_y\frac{\partial v}{\partial \eta} + \eta_z\frac{\partial w}{\partial \eta}) + W\frac{\partial \rho}{\partial \zeta} \\
&+ \rho(\zeta_x\frac{\partial u}{\partial \zeta} + \zeta_y\frac{\partial v}{\partial \zeta} + \zeta_z\frac{\partial w}{\partial \zeta}) + vis_1 = 0 \\
&\frac{\partial u}{\partial t} + d_2 + V\frac{\partial u}{\partial \eta} + \frac{1}{\rho}\eta_x\frac{\partial p}{\partial \eta} + W\frac{\partial u}{\partial \zeta} + \frac{1}{\rho}\zeta_x\frac{\partial p}{\partial \zeta} + vis_2 = 0 \\
&\frac{\partial v}{\partial t} + d_3 + V\frac{\partial v}{\partial \eta} + \frac{1}{\rho}\eta_y\frac{\partial p}{\partial \eta} + W\frac{\partial v}{\partial \zeta} + \frac{1}{\rho}\zeta_y\frac{\partial p}{\partial \zeta} + vis_3 = 0 \\
&\frac{\partial w}{\partial t} + d_4 + V\frac{\partial w}{\partial \eta} + \frac{1}{\rho}\eta_z\frac{\partial p}{\partial \eta} + W\frac{\partial w}{\partial \zeta} + \frac{1}{\rho}\zeta_z\frac{\partial p}{\partial \zeta} + vis_4 = 0 \\
&\frac{\partial p}{\partial t} + d_5 + V\frac{\partial p}{\partial \eta} + \gamma p(\eta_x\frac{\partial u}{\partial \eta} + \eta_y\frac{\partial v}{\partial \eta} + \eta_z\frac{\partial w}{\partial \eta}) + W\frac{\partial \rho}{\partial \zeta} \\
&+ \gamma p(\zeta_x\frac{\partial u}{\partial \zeta} + \zeta_y\frac{\partial v}{\partial \zeta} + \zeta_z\frac{\partial w}{\partial \zeta}) + vis_5 = 0
\end{aligned}
\tag{2.10}
$$

$$\begin{bmatrix} d_1 \\ d_2 \\ d_3 \\ d_4 \\ d_5 \end{bmatrix} = \begin{bmatrix} \frac{1}{c^2}[\frac{1}{2}(L_1+L_5)+L_2] \\ \frac{\xi_x}{2\beta\rho c}(L_5-L_1)-\frac{1}{\beta^2}(\xi_y L_3 +_z L_4) \\ \frac{\xi_y}{2\beta\rho c}(L_5-L_1)+\frac{1}{\beta^2\xi_x}[(\xi_x^2+\xi_z^2)L_3 -_z {}_y L_4] \\ \frac{\xi_z}{2\beta\rho c}(L_5-L_1)-\frac{1}{\beta^2\xi_x}[{}_y z L_3-(\xi_x^2+\xi_z^2)L_4] \\ \frac{1}{2}(L_1+L_5) \end{bmatrix}$$

In the above equation c is the speed of sound and $\beta = \sqrt{\xi_x^2+\xi_y^2+\xi_z^2}$. L_i represents the amplitude variations of the characteristic waves corresponding to the characteristic velocities, which are given by

$$\lambda_1 = U - C_\xi,$$

$$\lambda_2 = \lambda_3 = \lambda_4 = U,$$

$$\lambda_5 = U + C_\xi, (C_\xi = c\beta),$$

$$L_1 = (U-C_\xi)[-\frac{\rho c}{\beta}(\xi_x\frac{\partial u}{\partial \xi}+\xi_y\frac{\partial v}{\partial \xi}+\xi_z\frac{\partial w}{\partial \xi})+\frac{\partial p}{\xi}],$$

$$L_2 = U(c^2\frac{\partial \rho}{\partial \xi}-\frac{\partial p}{\partial \xi}),$$

$$L_3 = U(-\xi_y\frac{\partial u}{\partial \xi}+\xi_x\frac{\partial v}{\partial \xi}),$$

$$L_4 = U(-\xi_z\frac{\partial u}{\partial \xi}+\xi_x\frac{\partial w}{\partial \xi})\ and$$

$$L_5 = (U+C_\xi)[\frac{\rho c}{\beta}(\xi_x\frac{\partial u}{\partial \xi}+\xi_y\frac{\partial v}{\partial \xi}+\xi_z\frac{\partial w}{\partial \xi})+\frac{\partial p}{\xi}].$$

The above equations are used for neighbors of boundary points in the ξ direction. The equations for η and ζ directions are similar. In this way, the non-physical wave reflection can be effectively eliminated.

Blasius solution with enforced disturbunce is introduced into inlet as a laminar base inflow. The disturbance includes a two-dimensional T-S wave and a pair of conjugate three-dimensional T-S waves. The inflow has a form:

$$q = q_{lam} + A_{2d}q'_{2d}e^{i(\alpha_{2d}x-\omega t)} + A_{3d}q'_{3d}e^{i(\alpha_{3d}x\pm\beta y-\omega t)}$$

where $q = [u, v, w, T]^t$, q_{lam} is the Blasius solution for a two-dimensional laminar flat-plate boundary layer. $e^{i(\alpha_{2d}x-\omega t)}$ and $e^{i(\alpha_{3d}x\pm\beta y-\omega t)}$ are 2-D and 3-D pertubation waves (T-S wave). The streamwise wavenumber, spanwise wavenumber, frequency and amplitude are given as follows:

$$\lambda_{2d} = 0.29919 - i5.09586 \times 10^{-3},$$

$$\beta = \pm 0.5712,\ \omega = 0.114027,$$

$$A_{2d} = 0.03,\quad A_{3d} = 0.01$$

The T-S wave parameters are obtained by solving the compressible boundary layer stability equations [58].

2.3 Computational domain

The computational domain is displayed in Figure (2.1). The grid level is $1920\times128\times241$, representing the number of grids in streamwise (x), spanwise (y), and wall normal (z) directions. The grid is stretched in the normal direction and uniform in the streamwise and spanwise directions. The length of the first grid interval in the normal direction at the entrance is found to be 0.43 in wall units (Y^+=0.43). The parallel computation is accomplished through the Message Passing Interface (MPI) together with domain decomposition in the streamwise direction (Figure 2.2). The flow parameters, including Mach number, Reynolds number, etc. are listed in Table (1). Here, x_{in} represents the distance between leading edge and inlet, Lx, Ly, Lz_{in} are the lengths of the computational domain in x-, y-, and z-directions respectively, and T_w is the wall temperature.

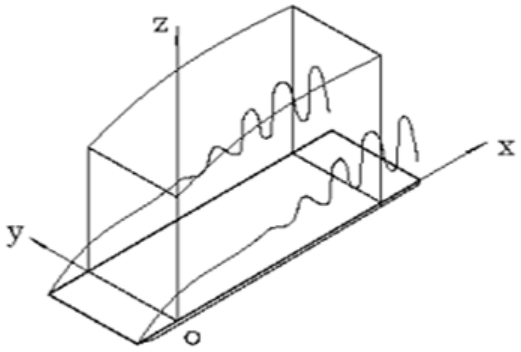

Figure 2.1: Domain decomposition along the streamwise direction in the computational space.

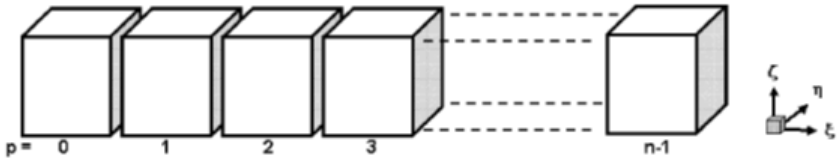

Figure 2.2: Computation domain.

Table 2.1: Flow parameters

M_∞	Re	x_{in}	Lx	Ly	Lz_{in}	T_w	T_∞
0.5	1000	$300.79\delta_{in}$	$798.03\delta_{in}$	$22\delta_{in}$	$40\delta_{in}$	273.15K	273.15K

2.4 Code validation

The DNS code "DNSUTA" has been validated by NASA Langley and UTA researchers [15, 37, 59, 60] carefully to make sure the DNS results are correct.

2.4.1 Comparison with linear theory

The spatial evolutions of the small disturbance imposed at the inlet are simulated. At the inlet boundary, the most amplified eigenmode of two-dimensional T-S waves is enforced. Figure (2.3) compares the velocity profile of the T-S wave given by our DNS results to linear theory [61]. Figure (2.4) is a comparison of the perturbation amplification

rate between DNS and LST. The agreement between linear theory and our numerical results is quite good.

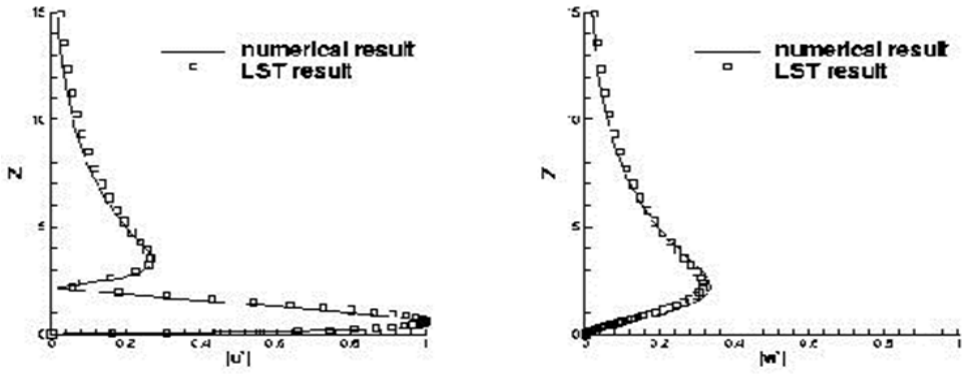

Figure 2.3: Comparison of the numerical and LST velocity profiles at $Re_x = 394300$.

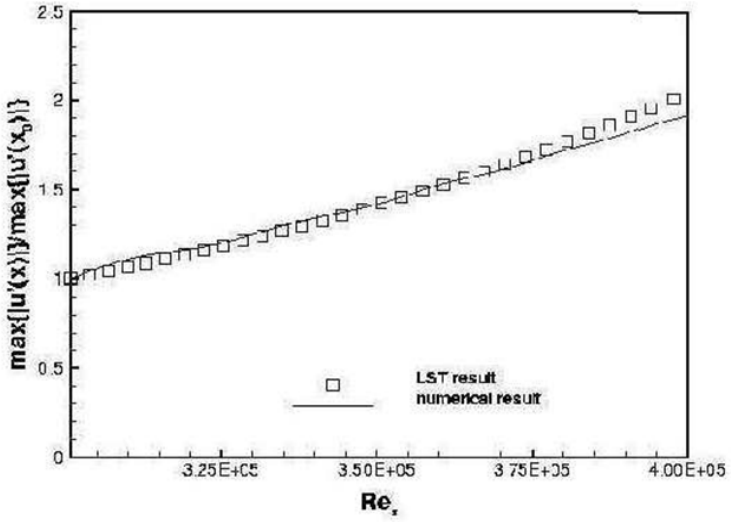

Figure 2.4: Comparison of the perturbation amplification rate between DNS and LST.

2.4.2 Grid convergence

The skin friction coefficient calculated from the time-averaged and spanwise-averaged profile for various streamwise locations on a coarse and fine grid is displayed in Figure2.5. The spatial evolution of skin friction coefficients of laminar flow is also plotted out for comparison. It is observed from these figures that the sharp growth of the skin-friction coefficient occurs after $x \approx 450\delta_{in}$, which is defined as the "onset point". The skin friction coefficient after transition is in good agreement with the flat-plate theory of turbulent boundary layer by Cousteix in 1989 (Ducros, 1996)[62]. Figures 2.5(a) and 2.5(b) also show that we get grid convergence in skin friction coefficients.

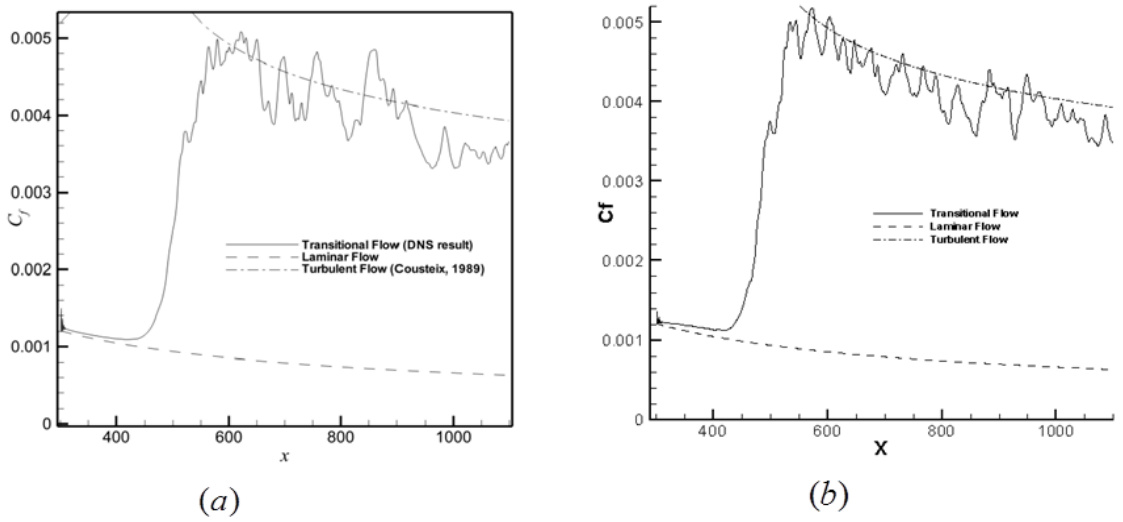

Figure 2.5: Streamwise evolutions of the time-and spanwise-averaged skin-friction coefficient: (a) Coarse grids ($960 \times 64 \times 121$), (b) Fine grids ($1920 \times 128 \times 241$).

2.4.3 Comparison with log law

Time-averaged and spanwise-averaged streamwise velocity profiles for various streamwise locations in two different grid levels are shown in Figure (2.6). The inflow velocity profiles at x=300.79δ_{in} is a typical laminar flow velocity profile. At x=632.33δ_{in} ,the mean

velocity profile approaches a turbulent flow velocity profile (Log law). This comparison shows that the velocity profile from the DNS results is turbulent flow velocity profile and the grid convergence has been realized.

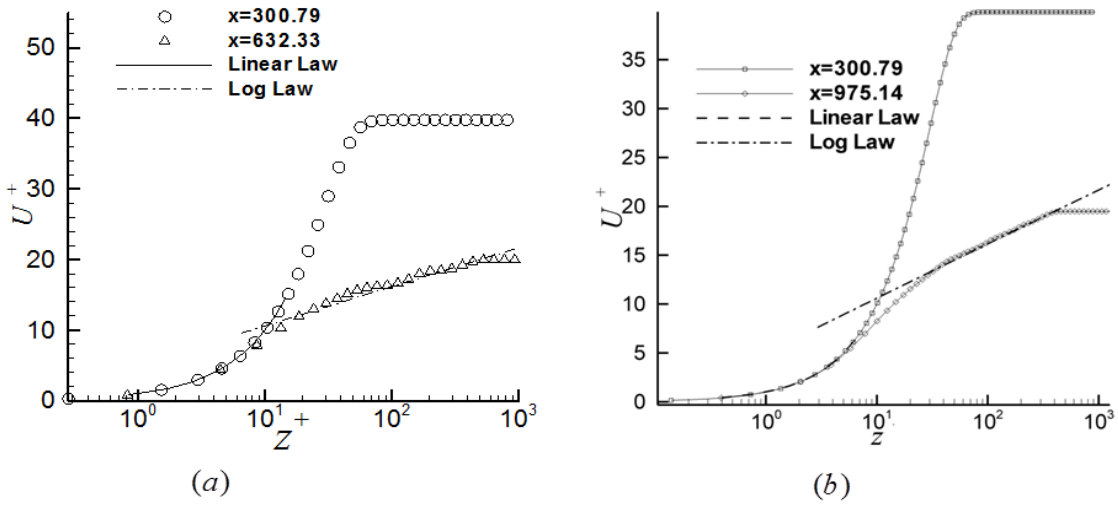

Figure 2.6: Log-linear plots of the time-and spanwise-averaged velocity profile in wall unit: (a) Coarse grids ($960 \times 64 \times 121$), (b)Fine grids($1920 \times 128 \times 241$).

2.4.4 Spectra and reynolds stress (velocity) statistics

Figure (2.7) shows the spectra in x- and y- directions. The spectra are normalized by z at location of $Re_x = 1.07 \times 10^6$ and $y^+ = 100.25$. In general, the turbulent region is approximately defined by $y^+ > 100$ and $y/\delta < 0.15$. In our case, The location of $y/\delta = 0.15$ for $Re_x = 1.07 \times 10^6$ is corresponding to $y^+ \approx 350$, so the points at $y^+ = 100$ and 250 should be in the turbulent region. A straight line with slope of -3/5 is also shown for comparison. The spectra tend to tangent to the $\kappa^{-3/5}$ law. The large oscillations of the spectra can be attributed to the inadequate samples in time when the average is computed.

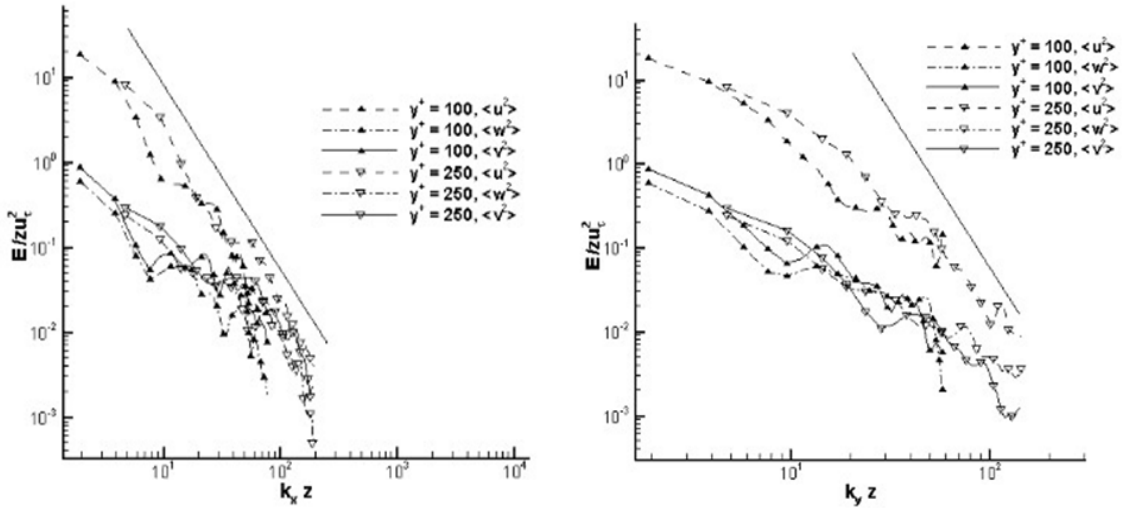

Figure 2.7: Spectral analysis: (a)Spectra in x direction, (b)Spectra in y direction.

2.4.5 Comparison with Other DNS

Although it doesn't make much sense to compare our DNS results with those given by Borodulin et al [45] quantitatively, it still can be found that the shear layer structures are very similar in two DNS computations in Figure (2.8).

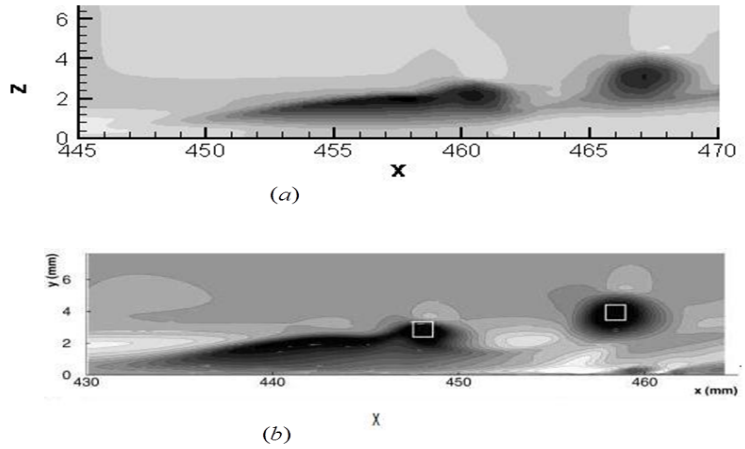

Figure 2.8: Qualitatively comparison of contours of streamwise velocity disturbance u in the (x, z)-plane (Light shades of gray correspond to high values): (a) Our DNS, (b) Boroduline et al. (2002).

2.4.6 U-shaped vortex in comparison with experimental results

Figure 2.9(a) (Guo et al. [50]) is an experimental investigation of the vortex structure including ring-like vortex and barrel-shaped head (U-shaped vortex). The vortex structures of the nonlinear evolution of T-S waves in the transition process are given by DNS in Figure 2.9(b). By careful comparison between the experimental work and DNS, we note that the experiment and DNS agree with each other in a detailed flow structure comparison.

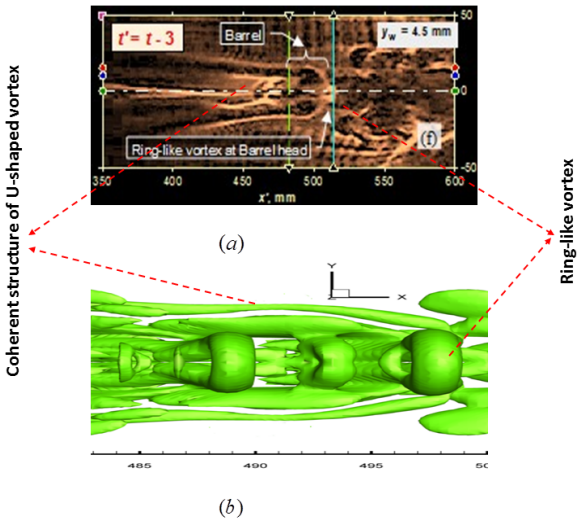

Figure 2.9: Qualitative vortex structure comparison with experiment: (a) Experimental results given by Guo et al(2010), (b) DNS result of U-shaped vortex.

2.5 Conclusion

We compared our DNS results with well known theories and then we tried find the qualitative similarities between our DNS results and experiments. There were interesting matching between those entirely different approach(Numerical simulation, theoretical and experimental data). It is impossible to be just a coincidence rather they may be some important clues:

1. Both DNS and experiment should be correct.
2. Although there are totally differences in inflow boundary conditions (random noises VS enforced T-S waves) and spanwise boundary conditions (non-periodic VS periodic) between experiment and DNS, the vortex structures are same. It means Turbulence has certain coherent structures (CS) for generation and sustenance.
3. No matter K-, H- or mixed types of transition, the final vortex structures are same.
4. There is an universal structure for late boundary layer transition.

CHAPTER 3

THE LAMINAR BOUNDARY-LAYER FLOW OVER A FLAT PLATE-BASE FLOW

3.1 Prandtl's boundary-layer concept

German scientist Ludwg Prandtl introduced the concept of aerodynamic boundary layer first on August 12, 1904 at the third International Congress of Mathematicians in Heidelberg, Germany [63]. The break through concept has enormous impact for the study of fluid dynamics. He made hypothesis that for the fluid with small viscosity (friction), the flow field around solid object moving along with the fluid may be divided into two regions as shown in Figure (3.1).

- A very thin layer very close to the body (known as boundary layer) where the fluid flow is dominated by viscosity so viscous effects are important along with inertia effects. Here velocity gradient along the normal wall ($\frac{\partial u}{\partial y}$) is very large so the viscous stress $\mu\frac{\partial u}{\partial y}$ has significantly important even if μ is very small.
- The region outside this layer (known as outer region) where the frictional effects (or viscous effects) may be considered as negligible and fluid is regarded as inviscid (potential flow or friction less flow). Here the velocity gradient normal to the wall ($\frac{\partial u}{\partial y}$) is very small or the viscous effect may be ignored completely.

Based on this boundary layer assumption, the Navier-Stokes equations which are elliptic partial differential equation (PDE) in behavior can be deducted into mathematically tractable from which is known as boundary layer equation. Further, using an order of magnitude analysis, the boundary layer equation subsequently can be simplified into parabolic ordinary differential equation [26]. The deduction of the boundary layer equations was one of the most important advances in fluid dynamics [64]. By making the boundary layer as-

sumption, the total flow field is divided into an inviscid portion -which simply can be solve by a number of methods- and the boundary layer, which is governed by an easier PDE. The closed form of solution is obtained on both cases.

Although there is no precise dividing line between the boundary layer and potential flow region, it is customary to define the boundary is that region where the fluid velocity parallel to the surface is less than 99% of the free stream velocity described by the potential flow theory.

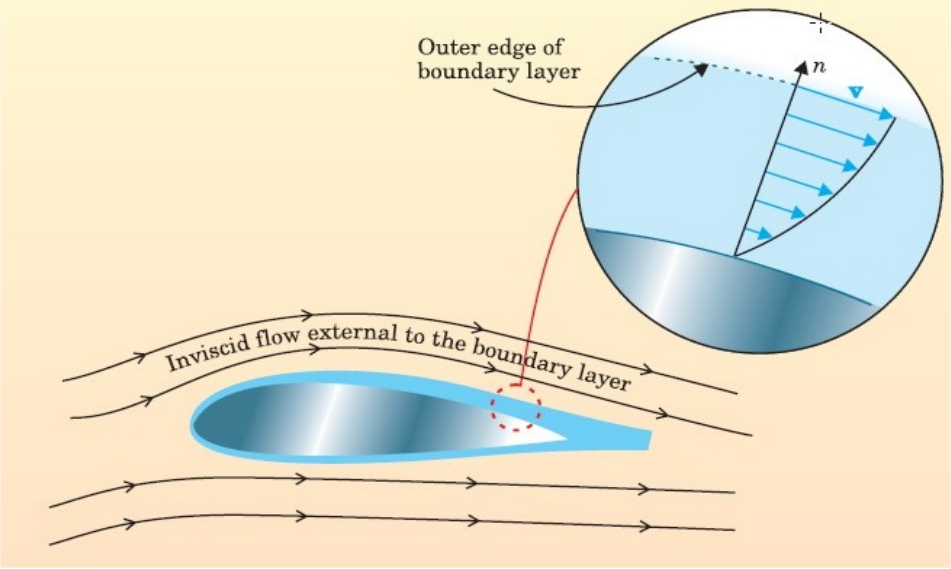

Figure 3.1: A sketch of boundary layer which was first introuduced by L. Prantel in 1905 [JD Anderson Jr - Physics Today, 2005]

Earlier than Prantel's 1905 paper, the Navier-Stoke equations were of very limited use in practical engineering problems due to the two main reasons:

- These equations are highly nonlinear PDE. Due to this fact, engineers weren't able to use classical approaches for solving PDEs such as superposition of several simple solutions, and the separation of variables approach where main flow properties such as velocity, density, pressure, temperature etc. are supposed to dependent each other.

- It was kind of impossible to calculate aerodynamic drag for any solid body immersing on any fluid since every flow property at a point on flow field is influenced by every other point in entire flow field. For instance,according to Navier-Stokes equations, the skin friction at a point on the nose of a jumbo jet will depend on the behavior of a point way downstream on the tail. This difficulty demands to solve the complex Navier-Stokes equations simultaneously, alone with the specific boundary conditions provided through the whole boundary of the flow.

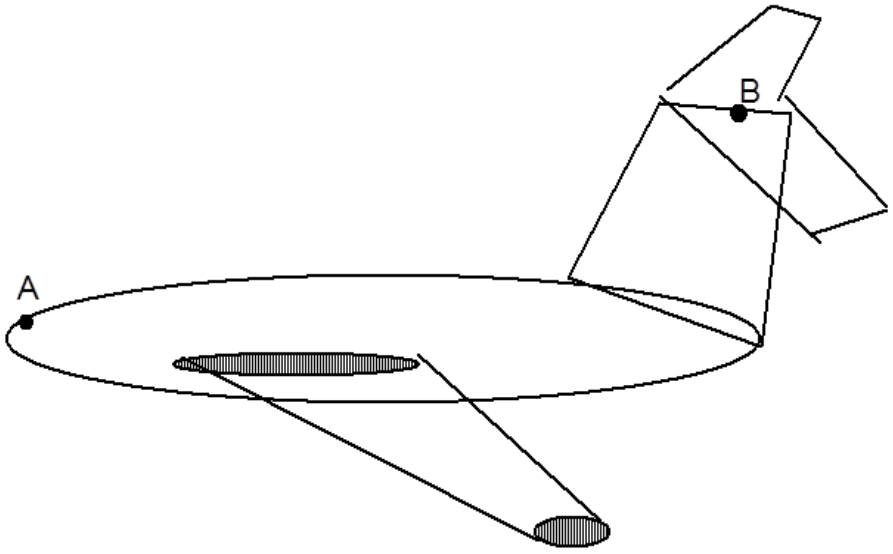

Figure 3.2: Flow properties at points A and B are coupled to each other because steady state form of Navier-Stokes equations are elliptic.

3.2 Compressible laminar flow over a flat plate

3.2.1 Governing equations

While deriving the two-dimensional compressible laminar boundary-layer equations, with(u,v) being the velocity components along parallel and normal to the wall, respectively. We assume the following approximations hold: $v << u$ and $\frac{\partial}{\partial x} << \frac{\partial}{\partial y}$ [29]. Then the gov-

erning equation for a steady, two-dimensional, compressible, laminar flow over a flat plate without body forces and bulk heat transfer and without a pressure gradient is as follows:

Continuity equation:

$$\boxed{\frac{\partial(\rho u)}{\partial x} + \frac{\partial(\rho v)}{\partial y} = 0} \tag{3.1}$$

Momentum equation:

$$\boxed{\begin{aligned} &\rho u\frac{\partial u}{\partial x} + \rho v\frac{\partial u}{\partial y} = \frac{\partial}{\partial y}(\mu\frac{\partial u}{\partial y}) \\ &\frac{\partial P}{\partial y} = 0 \end{aligned}} \tag{3.2}$$

Energy equation:

$$\boxed{\rho u\frac{\partial h}{\partial x} + \rho v\frac{\partial h}{\partial y} = \frac{\partial}{\partial y}(k\frac{\partial T}{\partial y}) + \mu(\frac{\partial u}{\partial y})^2} \tag{3.3}$$

An equation of state:

$$\boxed{p = \rho RT} \tag{3.4}$$

$$\boxed{h = c_p T} \tag{3.5}$$

where, $h = e + \frac{p}{\rho}$ is the fluid enthalpy. From the y-momentum equation, we also note that pressure is independent in normal direction of the flow field that means $p = p(x)$. There are five unknowns(u, v, ρ, h, T) and five equations. μ and k are properties of the fluid which depend upon temperature. That is $\mu = \mu(T)$ and $k = k(T)$.

3.2.2 Boundary conditions

The boundary conditions at the wall, i.e., y=o are given by the no-slip velocity condition with or without mass transfer or heat transfer.

$$At\ \ y = 0 :\ \ u = 0,\ \ v = 0,\ \ T = T_w$$

At the edge of the boundary-layer, we assume that the viscous flow inside the boundary-layer smoothly change into the inviscid flow outside the boundary-layer.

$$At\ \ y \to \infty : u \to U_e, T \to T_e$$

where the subscript e is used for conditions at the edge of the boundary layer.

Let us introduce nondimensional variables as follow:

$$\bar{u} = \frac{u}{U_e} \qquad \bar{v} = \frac{v}{U_e} \qquad \bar{x} = \frac{x}{L} \qquad \bar{y} = \frac{y}{L}$$

$$\bar{p} = \frac{p}{\rho_e U_e^2} \qquad \bar{h} = \frac{h}{h_e} \qquad \bar{\mu} = \frac{\mu}{\mu_e} \qquad \bar{\rho} = \frac{\rho}{\rho_e}$$

where, L is the characteristics length, U_e is the flow velocity which is aligned with x-direction.

Substituting the above quantities into Equations (3.1) to (3.3), we get

$$\frac{\partial(\bar{\rho}\bar{u})}{\partial\bar{x}} + \frac{\partial(\bar{\rho}\bar{v})}{\partial\bar{y}} = 0$$

$$\bar{\rho}\bar{u}\frac{\partial\bar{u}}{\partial\bar{x}} + \bar{\rho}\bar{v}\frac{\partial\bar{u}}{\partial\bar{y}} = \frac{1}{Re}\frac{\partial}{\partial\bar{y}}(\bar{\mu}\frac{\partial\bar{u}}{\partial\bar{y}})$$

$$\frac{\partial\bar{P}}{\partial\bar{y}} = 0$$

$$\bar{\rho}\bar{u}\frac{\partial\bar{h}}{\partial\bar{x}} + \bar{\rho}\bar{v}\frac{\partial\bar{h}}{\partial\bar{y}} = \frac{1}{Re}\frac{1}{Pr}\frac{\partial}{\partial\bar{y}}(\bar{k}\frac{\partial\bar{T}}{\partial\bar{y}}) + \frac{(\gamma-1)M_e^2}{Re}\bar{\mu}(\frac{\partial\bar{u}}{\partial\bar{y}})^2$$

where $Re = \frac{\rho_e U_e L}{\mu_e}$ and $(\gamma-1)M_e^2 = \frac{U_e^2}{h_e}$

It can be clearly noted from the nondimensional energy equation that the work done due to compression and viscous dissipation play role as the Mach number of the external flow increases.

3.2.3 Energy equation in terms of enthalpy

It is sometimes convenient to rewrite the energy equation in terms of the total enthalpy , $H = h + \frac{V^2}{2}$,as the dependent variable in the energy equation, other than the static enthalpy as written in Equation (3.3). Here we assume the y component of velocity, v, is very small. So, $H = h + \frac{V^2}{2} = h + (\frac{u^2+v^2}{2}) \approx h + \frac{u^2}{2}$.

Now multiply Equation (3.2) by u, and add to Equation (3.3)

$$\rho u\frac{\partial(u^2/2)}{\partial x}+\rho v\frac{\partial(u^2/2)}{\partial y}=u\frac{\partial}{\partial y}(\mu\frac{\partial u}{\partial y}) \tag{3.6}$$

Adding Equations (3.3) and (3.6), we get

$$\rho u\frac{\partial(h+u^2/2)}{\partial x}+\rho v\frac{\partial(h+u^2/2)}{\partial y}=\frac{\partial}{\partial y}(k\frac{\partial T}{\partial y})+\mu(\frac{\partial u}{\partial y})^2+u\frac{\partial}{\partial y}(\mu\frac{\partial u}{\partial y}) \tag{3.7}$$

From perfect gas assumption, $dh = c_p dT$, we have

$$\frac{\partial T}{\partial y}=\frac{1}{c_p}\frac{\partial h}{\partial y}=\frac{1}{c_p}\frac{\partial}{\partial y}(H-\frac{u^2}{2}) \tag{3.8}$$

Substituting the Equation (3.8) into Equation (3.7), we get

$$\rho u\frac{\partial H}{\partial x}+\rho v\frac{\partial H}{\partial y}=\frac{\partial}{\partial y}[\frac{k}{c_p}\frac{\partial}{\partial y}(H-\frac{u^2}{2})]+\mu(\frac{\partial u}{\partial y})^2+u\frac{\partial}{\partial y}(\mu\frac{\partial u}{\partial y}) \tag{3.9}$$

Also,

$$\frac{k}{c_p}\frac{\partial}{\partial y}(H-\frac{u^2}{2})=\frac{\mu k}{\mu c_p}\frac{\partial}{\partial y}(H-\frac{u^2}{2})=\frac{\mu}{Pr}(\frac{\partial H}{\partial y}-u\frac{\partial u}{\partial y}) \tag{3.10}$$

And

$$\mu(\frac{\partial u}{\partial y})^2+u\frac{\partial}{\partial y}(\mu\frac{\partial u}{\partial y})=\frac{\partial}{\partial y}(\mu u\frac{\partial u}{\partial y}) \tag{3.11}$$

finally, substituting the Equations (3.9), (3.10) and (3.11) into the Equation (3.8) and simplifying we get

$$\boxed{\rho u\frac{\partial H}{\partial x}+\rho v\frac{\partial H}{\partial y}=\frac{\partial}{\partial y}[\frac{\mu}{pr}\frac{\partial H}{\partial y}+(1-\frac{1}{Pr})+\mu u\frac{\partial u}{\partial y}]} \tag{3.12}$$

The nonlinear partial differential Equations (3.1), (3.2) and (3.12) can be considered as the governing equations for laminar compressible flow over a flat plate without any pressure gradient.

3.2.4 Similarity solutions

Although the compressible boundary layer Euations (3.2), (3.2) and (3.12) can be directly attacked by finite-difference methods, similarity transformation give easier solutions. As for incompressible boundary layers, a number of beautiful transformations for incompressible flows has been developed by earlier researchers. Here, we discuss only one of these transformations, the Illingworth transformation, given by Illingworth in 1950 [65]. The compressible stream function $\psi(x, y)$ is defined as

$$\begin{aligned} \frac{\partial \psi}{\partial y} &= \rho u \\ \frac{\partial \psi}{\partial x} &= -\rho v \end{aligned} \tag{3.13}$$

The Equation (3.13) automatically satisfies the continuity Equation (3.1). Now, substituting the Equation (3.13) into momentum Equation (3.2) and Energy Equation (3.12), we get

$$\frac{\partial \psi}{\partial y}\frac{\partial}{\partial x}(\frac{1}{\rho}\frac{\partial \psi}{\partial y}) - \frac{\partial \psi}{\partial x}\frac{\partial}{\partial y}(\frac{1}{\rho}\frac{\partial \psi}{\partial y}) = \frac{\partial}{\partial y}[\mu\frac{\partial}{\partial y}(\frac{1}{\rho}\frac{\partial \psi}{\partial y})] \tag{3.14}$$

$$\frac{\partial \psi}{\partial y}\frac{\partial H}{\partial x} - \frac{\partial \psi}{\partial x}\frac{\partial H}{\partial y} = \frac{\partial}{\partial y}[\frac{\mu}{pr}\frac{\partial H}{\partial y} + (1 - \frac{1}{Pr}) + \mu(\frac{1}{\rho}\frac{\partial \psi}{\partial y})\frac{\partial}{\partial y}(\frac{1}{\rho}\frac{\partial \psi}{\partial y})] \tag{3.15}$$

The corresponding boundary conditions are modified into

$$\begin{aligned} &At\ y = 0: \ \frac{\partial \psi}{\partial x} = 0,\ \frac{\partial \psi}{\partial y} = 0,\ T = T_w \\ &At\ y \to \infty: \ \frac{\partial \xi}{\partial x} \to U_e, \quad T \to T_e \end{aligned} \tag{3.16}$$

As in incompressible flow case, we try to seek a self-similar transformations and the corresponding similar solutions by changing the independent variables(x,y) to (ξ, η); however, the transformed independent variables are introduced slightly differently as follows:

$$\xi = \int_0^x \rho_e(x) U_e(x) \mu_e(x)\, dx = \xi(x) \tag{3.17}$$

$$\eta = \eta(x, y) \tag{3.18}$$

Whereas, the dependent variable transformations are introduced as follows:

$$\psi(x,y) = \sqrt{2\xi} f(\eta) \tag{3.19}$$

$$u(x,y) = U_e(\xi) f^{'}(\eta) \tag{3.20}$$

$$H(x,y) = H_e(\xi) g(\eta) \tag{3.21}$$

The relation between independent and dependent variable transformation can be derived by using the definitions of compressible stream functions in Equation (3.13) :

$$\frac{\partial \psi}{\partial y} = \sqrt{2\xi}\frac{\partial \eta}{\partial y} f^{'}(\eta) = \rho u = \rho_e(x) U_e(x) f^{'}(\eta) \tag{3.22}$$

Comparing the above Equation (3.22), we get:

$$\frac{\partial \eta}{\partial y} = \frac{U_e(x)}{\sqrt{2\xi}}\rho \tag{3.23}$$

Integrating The Equation (3.23),

$$\eta = \frac{U_e}{\sqrt{2\xi}} \int_0^y \rho \, dy \tag{3.24}$$

Using the chain rule, we get

$$\frac{\partial}{\partial x} = \frac{\partial}{\partial \xi}\frac{\partial \xi}{\partial x} + \frac{\partial}{\partial \eta}\frac{\partial \eta}{\partial x} \tag{3.25}$$

$$\frac{\partial}{\partial y} = \frac{\partial}{\partial \xi}\frac{\partial \xi}{\partial y} + \frac{\partial}{\partial \eta}\frac{\partial \eta}{\partial y} \tag{3.26}$$

From the Equation (3.17), we have

$$\frac{\partial \xi}{\partial x} = \xi^{'}(x) = \rho_e(x) U_e(x) \mu_e(x) \tag{3.27}$$

$$\frac{\partial \xi}{\partial y} = 0 \tag{3.28}$$

(Here, we don't have to calculate $\frac{\partial \eta}{\partial x}$ since this term will cancel in our equations)

Now, substituting Equations (3.27) and (3.28) into the Equations (3.25) and (3.26), we have

$$\frac{\partial}{\partial x} = \rho_e U_e \mu_e \frac{\partial}{\partial \xi} + \frac{\partial}{\partial \eta}\frac{\partial \eta}{\partial x} \tag{3.29}$$

$$\frac{\partial}{\partial y} = \frac{\partial}{\partial \eta}\frac{U_e}{\sqrt{2\xi}}\rho \tag{3.30}$$

Now, let us calculate the following terms:

$$\begin{aligned} v &= -\frac{1}{\rho}\frac{\partial \psi}{\partial x} \\ &= -\frac{1}{\rho}[\rho_e U_e \mu_e \frac{\partial \psi}{\partial \xi} + \frac{\partial \psi}{\partial \eta}\frac{\partial \eta}{\partial x}] \\ &= -\frac{1}{\rho}[\frac{\rho_e \mu_e U_e}{\sqrt{2\xi}} f(\eta) + \sqrt{2\xi} f^{'}(\eta)\frac{\partial \eta}{\partial x}] \end{aligned} \tag{3.31}$$

$$\begin{aligned} \frac{\partial u}{\partial x} &= \rho_e U_e \mu_e \frac{\partial u}{\partial \xi} + \frac{\partial u}{\partial \eta}\frac{\partial \eta}{\partial x} \\ &= U_e f^{''}(\eta)\frac{\partial \eta}{\partial x} \end{aligned} \tag{3.32}$$

Again,

$$\begin{aligned} \frac{\partial u}{\partial y} &= \frac{\partial u}{\partial \eta}\frac{U_e}{\sqrt{2\xi}}\rho \\ &= \frac{U_e^2}{\sqrt{2\xi}}\rho f^{'}(\eta) \end{aligned} \tag{3.33}$$

And,

$$\begin{aligned} \frac{\partial}{\partial y}(\mu\frac{\partial u}{\partial y}) &= \frac{\partial}{\partial \eta}[\mu\frac{U_\infty^2(x)}{\sqrt{2\xi}}\rho f^{'}(\eta)]\frac{U_\infty(x)}{\sqrt{2\xi}}\rho \\ &= \rho\mu f^{''}(\eta)\frac{U_e^2}{2\xi} \\ &= \frac{\rho\mu U_e^2}{2\xi} f^{''}(\eta) \end{aligned} \tag{3.34}$$

Now, substituting the Equations (3.31), (3.32), (3.33)and Equation(3.34) into the Equation (3.2, we get

$$\rho U_e^2 f^{'} f^{''}\frac{\partial \eta}{\partial x} - \frac{1}{2\xi}\rho\rho_e\mu_e U_e^3 f f^{''} - \rho U_e^2 f^{'} f^{''}\frac{\partial \eta}{\partial x} = (\rho\mu f^{''})^{'}\frac{U_e^3\rho}{2\xi}$$

$$\rho\frac{U_e^3}{2\xi}[(\rho\mu f'')' + \rho_e\mu_e f f''] = 0$$

$$(\rho\mu f'')' + \rho_e\mu_e f f'' = 0$$

$$(\frac{\rho\mu}{\rho_e\mu_e}f'')' + f f'' = 0 \tag{3.35}$$

The boundary-layer energy Equation (3.12) can also be reduced to an ordinary differential equation. For this, we split the enthalpy into a magnitude times a shape as:

$$H(x,y) = H_e(\xi)g(\eta) \tag{3.36}$$

By using the Equations (3.36), (3.29) and (3.30), we can immediately calculate the following expressions:

$$\begin{aligned}\frac{\partial H}{\partial x} &= \rho_e U_e \mu_e \frac{\partial H}{\partial \xi} + \frac{\partial H}{\partial \eta}\frac{\partial \eta}{\partial x} \\ &= H_e g'(\eta)\frac{\partial \eta}{\partial x}\end{aligned} \tag{3.37}$$

Similarly,

$$\begin{aligned}\frac{\partial H}{\partial y} &= \frac{\partial H}{\partial \eta}\frac{U_e}{\sqrt{2\xi}}\rho \\ &= \frac{\rho U_e H_e}{\sqrt{2\xi}}g'(\eta)\end{aligned} \tag{3.38}$$

Substituting the Equations (3.37) and (3.38) into the Equation (3.12) or (3.15), we get:

$$\rho U_e f' H_e g'\frac{\partial \eta}{\partial x} - [\frac{\rho_e\mu_e U_e}{\sqrt{2\xi}}f + \sqrt{2\xi}f'(\eta)\frac{\partial \eta}{\partial x}]\frac{\rho U_e H_e}{\sqrt{2\xi}}g'$$

$$= [\frac{\mu}{Pr}\frac{\rho U_e H_e}{\sqrt{2\xi}}g' + (1-\frac{1}{Pr})\frac{\rho\mu U_e^3}{\sqrt{2\xi}}f' f"]'\frac{\rho U_e}{\sqrt{2\xi}}$$

$$(\frac{\rho\mu}{\rho_e\mu_e}\frac{1}{Pr}g')' + fg' + \frac{U_e^2}{H_e}[(1-\frac{1}{Pr})\frac{\rho\mu}{\rho_e\mu_e}f' f"]' = 0 \tag{3.39}$$

Hence the Equations (3.2) and (3.12) transform into the ordinary differential equations as

$$\boxed{(\frac{\rho\mu}{\rho_e\mu_e}f'')' + f f'' = 0} \tag{3.40}$$

$$\boxed{(\frac{\rho\mu}{\rho_e\mu_e}\frac{1}{Pr}g')' + fg' + \frac{U_e^2}{H_e}[(1-\frac{1}{Pr})\frac{\rho\mu}{\rho_e\mu_e}f' f"]' = 0} \tag{3.41}$$

With the corresponding boundary conditions from the Equation (3.16)

$$\begin{aligned} &At\ \eta = 0: \ \ f = 0,\ \ f^{'} = 0,\ \ g = g_w \\ &At\ \eta \to \infty: \ \ f^{'} = 1, \quad g = 1 \end{aligned} \tag{3.42}$$

Where, the prime denotes the differentiation with respect to η. The product $\rho\mu$ is a variable quantity and mainly depends upon temperature.

3.2.5 Numerical solution

If we carefully examine the the Equations (3.40) and (3.41), we find that these equations are ordinary differential equations which are coupled to each other through the quantities $\rho\mu, f, f^{'} and\ f^{"}$. These equations requires to be solved simultaneously. In order to solve these Equations (3.40) and (3.41), we use classical nonlinear shooting technique. As we see Equation (3.40) is third order ordinary differential equation, we need three boundary conditions at $\eta = 0$. But we have only two conditions, $f = f^{'} = 0$. Therefore, we consider another condition $f^{"}(0)$ and iterate until the boundary condition at edge $f^{'}(\eta) = 1$ is obtained. Again, Equation (3.41) is second order differential equation. In order to solve this equation along the boundary layer it requires two boundary conditions at the wall. The problem is we have only one boundary condition, $g(0) = g(w)$. So, we assume $g^{'}(0)$ and iterate the Equation (3.41) until the outer boundary condition, $g^{'} = 1$ is achieved.

The similarity solution of Equations (3.40) and (3.41) of the velocity and temperature profiles for a laminar compressible flow over flat plate is given in the Figures (3.3) and (3.4) respectively. Figure (3.5) is the velocity profile for compressible boundary-layer velocity profile over a flat with insulated wall given by Van Drist (1952) [66].

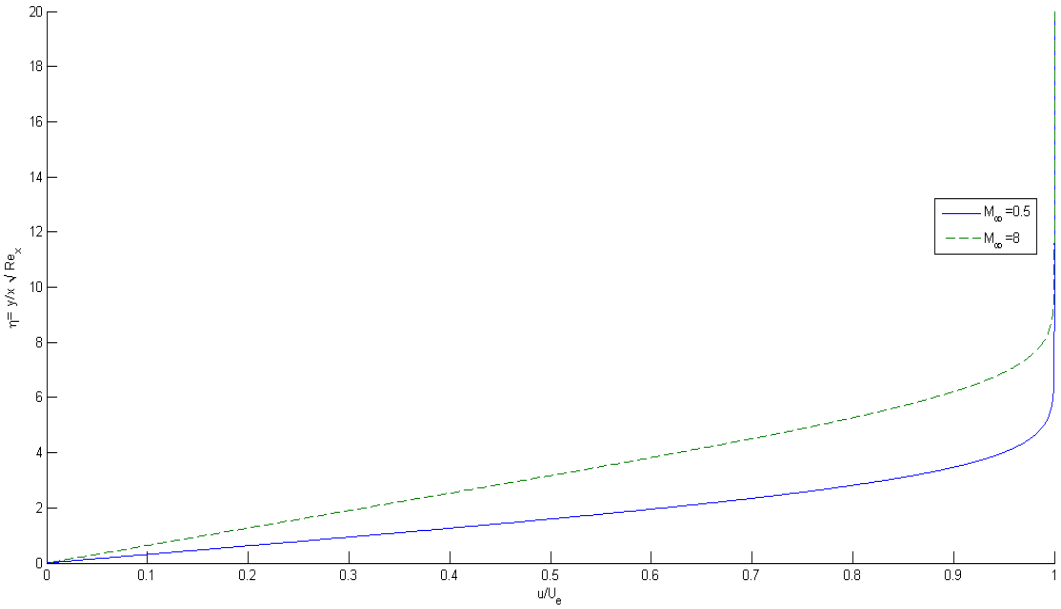

Figure 3.3: Velocity profile in a compressible laminar boundary-layer over our flat plate (adabatic wall).

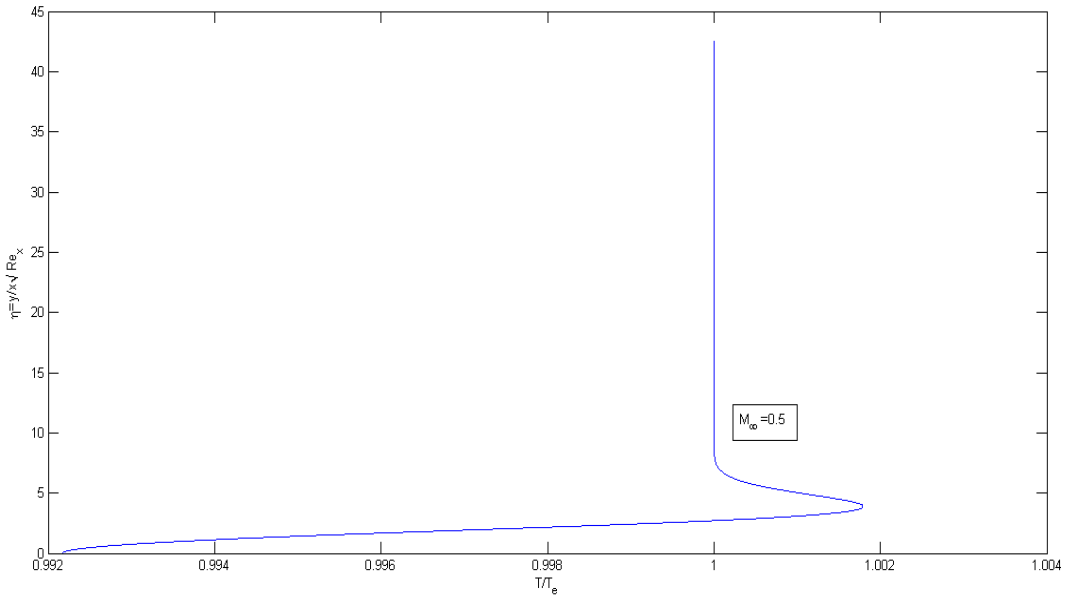

Figure 3.4: Temperature profile in a compressible laminar boundary-layer over our flat plate (adabatic wall).

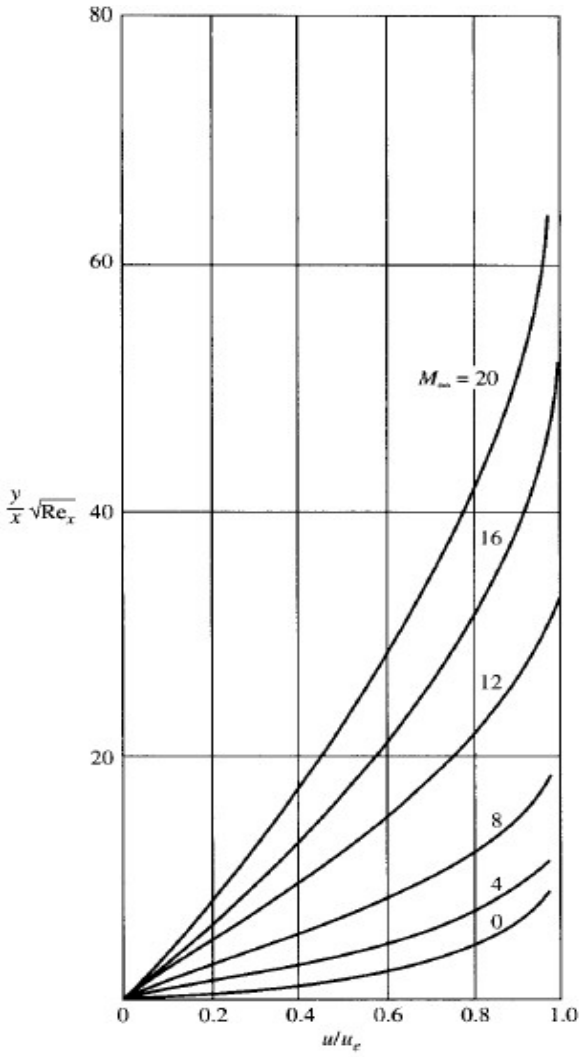

Figure 3.5: Velocity profile in a compressible laminar boundary-layer over an insulated flat plate [Van Drist (1952].

3.3 Conclusion

As we used 2-D compressible laminar boundary layer solution as a "base flow" of our DNS, so, the base flow was thoroughly investigated in this chapter. A numerical self-similar solution of viscous compressible laminar flow was obtained by using classical shooting method which matches with the earlier numerical simulation by Van Drist (1952).

CHAPTER 4

ORIGIN OF THE CHAOS IN LATE BOUNDARY-LAYER TRANSITION

4.1 Introduction

It is now well known that the late stages of the laminar-turbulent transition in boundary layer is dominated by complex and multi-scaled flow dynamics and occurrence of universal coherent vortical structures such as horseshoe, hairpin and ring-like vortices [67, 68, 69]. These vortical structures are robust and persist for long time [6]. Actually, these ring-like vortices travel downstream without breakdown until the sufficient amount of dissipation comes into play. That means,even if the well developed turbulent flow seems very entangled and chaotic but still the universal structures are present there. Under this circumstance it is reasonable to consider the basic flow structure between late stage of transitional flow and developed turbulence are likely not fundamentally different. Since the transitional flow structure is less chaotic and easier for analysis which may be helpful to better understand wall-bounded turbulent shear flow and eventually modeling such kind of flow. The focus of our present work is on the late (essentially nonlinear) stages of the transition.

In contrast to the earlier stages of the transitional process which can be sufficiently described by linear and secondary stability theory, the super late stages of transition-where the state laminar flow changes into turbulent one- is not yet as clearly understood and it's numerical simulation requires large computer resources. Although the laminar-turbulent transition is very sensitive to details of inflow, it is still important to locate the earliest location of turbulence for a particular inflow condition. In order to shed some light on the late stage transition, we thoroughly analyze our huge amount of data obtained by new high

order DNS and try to locate as earliest as possible streamwise location originating the chaos (turbulent spots) for a particular inflow conditions [70].

4.2 Nature of the non-linear flow in late stages of the laminar-turbulent transition

To gain additional insight for the mechanism of chaos formation process in very late stage of the transition, here we present a short review of origination and evolution of coherent vertical structures which are produced by interaction of non-linear Tollmien-Schlichting (T-S) waves at the late stage. Blasius solution is introduced into inlet as a base inflow along with artificial 2-D and 3-D perturbations. For identification of vortex structures in viscous flow, we use λ_2-eigenvalue technology developed by Jeong and Hussain [71]. This method uses the eigenvalues of the symmetric 3×3 tensor

$$M_{ij} := \sum_{k=1}^{3} \Omega_{ik}\Omega_{kj} + S_{ik}S_{kj},$$

where,

$$\Omega_{ij} := \frac{1}{2}(\frac{\partial u_i}{\partial x_j} + \frac{\partial u_j}{\partial x_i}) \ and \ S_{ij} := \frac{1}{2}(\frac{\partial u_i}{\partial x_j} - \frac{\partial u_j}{\partial x_i})$$

represent the symmetric and anti-symmetric components of the velocity gradient tensor, $\bigtriangledown u$. If the three real eigen-value of M are listed as $\lambda_1 \leq \lambda_2 \leq \lambda_3$, then any region for which λ_2 corresponds to a vortex core. Figure (4.1) is the evolution of time dependent vortical structures at the stage of transition. Actually, the late stage of transition starts with development of two pairs of counter-rotating Λ (horse shoe)-vortices at time $t = 6T$ as shown in Figure 4.1(a). These structures are rather short at the beginning ($x = 412 - 420\delta_{in}$). They are continuously stretching during their evolution- the velocity for top and bottom is different- and become much larger while moving downstream. While moving further downstream , Ω-(hairpin) vortices appear. Perfectly circular and perpendicular ring-

like vortices are generated by the interaction of primary and secondary streamwise vortices and they are gradually lifted up due to boundary layer mean velocity profile [72].

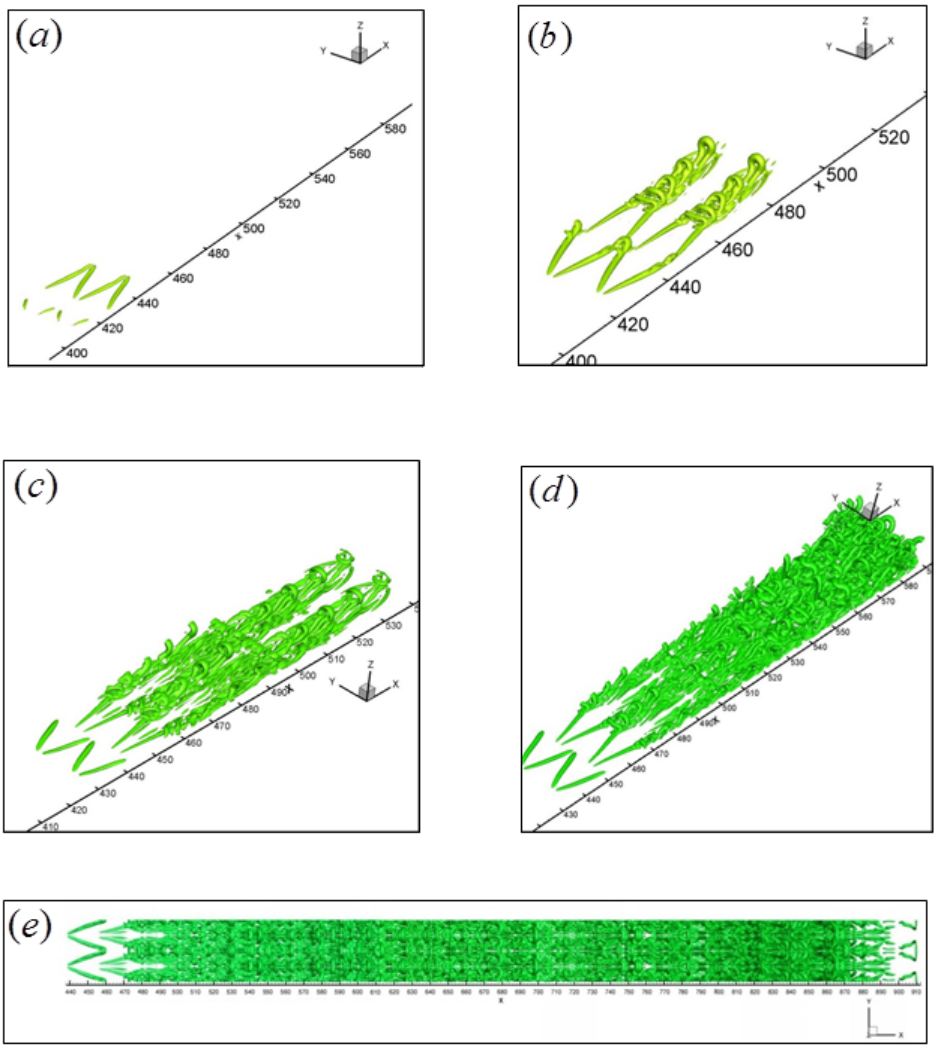

Figure 4.1: Evolution of vortex structure at the late-stage of transition(Where T is the period of T-S wave); (a) t=6.0T, (b) t=7T, (c) t=8T, (d) t=10.3T, and (e) t=17.0T **(For the purpose of clear visualization, the color of vortex sturucture is changed after t= 8T)**

Two important phenomena, namely "sweep" (downdraft motions) [73, 74] and "ejection" (updraft motion) [50, 73] represent the primary constitutive events in late transitional flow which are connected with ring-like vortices. When the first sweep motion between

legs of Λ and the second sweep from the center of ring-like vortices mix with each other, becomes much stronger downdraft motion and bring low speed flow from the boundary-layer bottom to high speed zone near the inviscid area causing high shear layer just above the ring legs. This shear layer is very unstable. Hence multiple ring-like vortices are formed by following first Helmholtz vortex conservation law as shown in Figure 4.1(b). For detail mechanism [75, 76]. From Figure 4.1(c), we observe that second ring cycle overlaps first cycle ($x = 472 - 490\delta_{in}$). This phenomenon will be described in more detail in section 5.3. The coherent vertical structures which were demonstrating very salient feature at the beginning , now started to entangle each other. As we see from Figure 4.1(d), the third level cycle just starts to overlap previous cycles in time step $t = 10.3T$ at $x \approx 500$. The complicated and nonlinear flow field in the late stage of time can be visualized as Figure 4.1(e).

4.3 Chaos starts from Second ring cycle nearly at middle in both streamwise and spanwise directions

Here we mainly focused on the flow field which is viable through our DNS. Figure 4.2(a) and (b) are top and bottom view of vortices structure at $t = 16.25T$. We can clearly see from the figure 4.2(a) that the top ring structures are symmetric. To investigate the symmetry of the bottom structure, a slice in streamwise direction of flow field has inserted at very bottom. From figure 4.3(a) and 4.3(b) it looks that the bottom structure is still symmetric.

To further investigate the bottom structure at the above mentioned time, three different slices are considered at three different position ($z = 0.4;\ z = 1.5; and z = 2.3$). While taking consideration of iso-surface of pressure for these slices, it can be clearly claimed

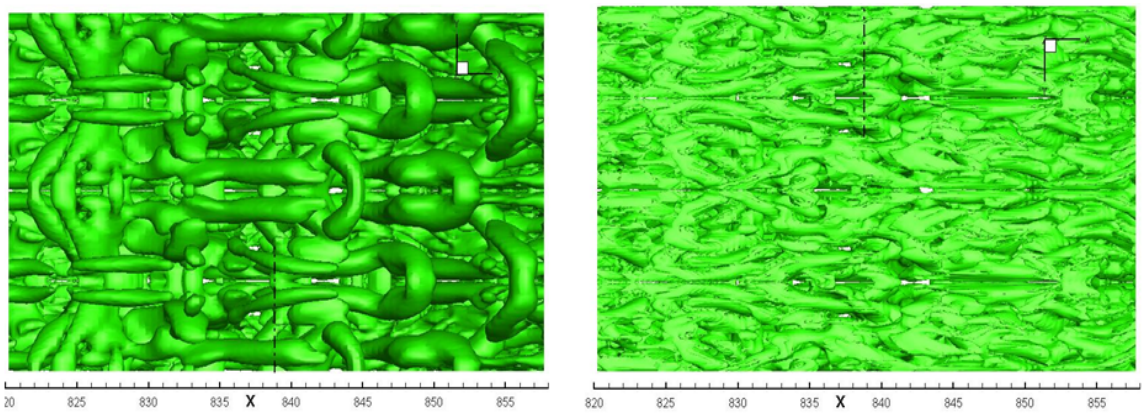

Figure 4.2: Asymmetric phenomenon started in middle while top and bottom still preserve symmetry (t=16.75T); (a) Top view, (b) Bottom view.

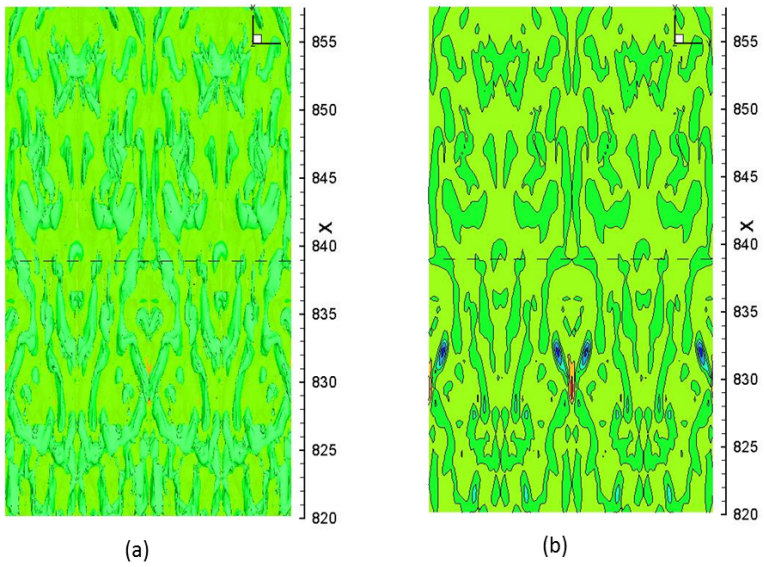

Figure 4.3: Bottom ring cycle structure $(t = 16.75T)$; (a) Bottom view with a slice, (b) Bottom slice with flood and line.

From the Figures 4.4(a),(b) and (c) that the bottom ring cycles are also asymmetric and periodic (in spanwise direction).

Meanwhile, to investigate the mechanism of flow chaos in spanwise direction, a slice from Figure 4.2(a) is chosen in stremwise direction at $x = 838.9\delta_{in}$. With development of

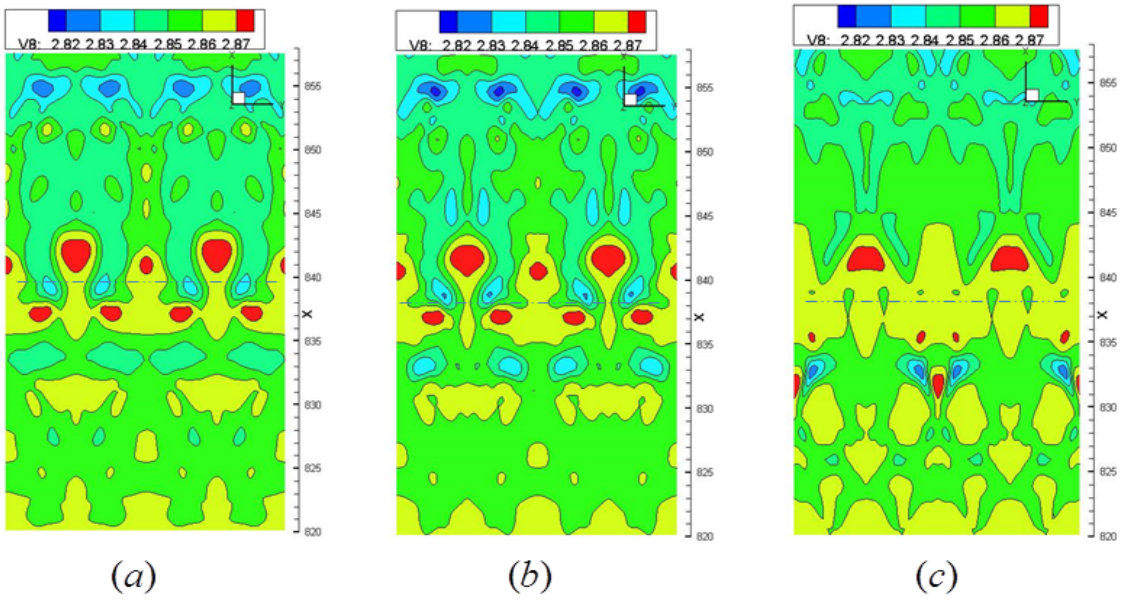

Figure 4.4: Bottom ring cycle structure $(t = 16.75T)$; (a) $z = 0.4$, (b) $z = 1.5$, (c) $z = 2.3$.

advanced tools for flow visualization in our modern era of research, stream-traces are useful to check intensity of vortices. We can clearly see from Figure 4.5(a) that the two vortex rings inside left and right white rectangular boxes are generated with different intensity of verticity.Figure 13(b) is the enlarged cross section of Figure 4.5(b). However, all other vortices have same magnitude of intensity.

To justify that the two vortices indeed have different intensities, we further check two other variables namely pressure and spanwise vorticity (Ω_y). From Figure 4.6(a), we see that there is less pressure at the left vortex ring position in black rectangle than in the right black rectangle. Also, from Figure 4.6(b), we can visualize that left vortex ring has greater intensity of spanwise vorticity than the right vortex ring. This observation is consistent with the theory that vortex core always has low pressure.

We further try to confirm our claim (subsection 3.2) by using 3-dimensional coherent vertical structures. Here, we cut our domain in such a way that the visible tail of vertical structure starts from exactly the same slice in Figure (4.5) and (4.6). Figure (4.7) is tail

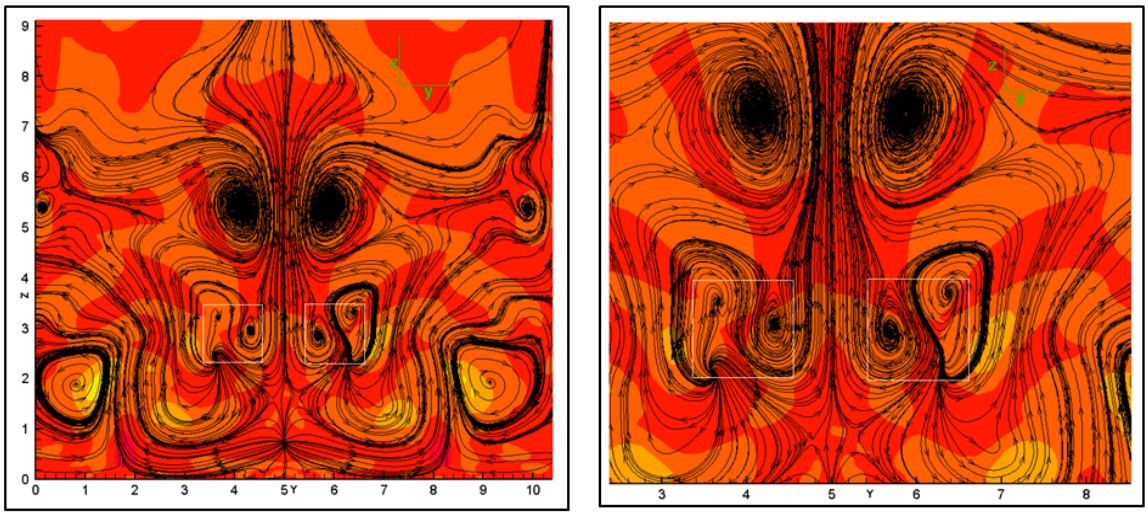

(a) (b)

Figure 4.5: Chaos started in middle while top and bottom still preserve symmetry ($t = 16.75T$); (a) Cross-section of λ_2 (b) Enlarged cross-section of λ_2 and stream-trace

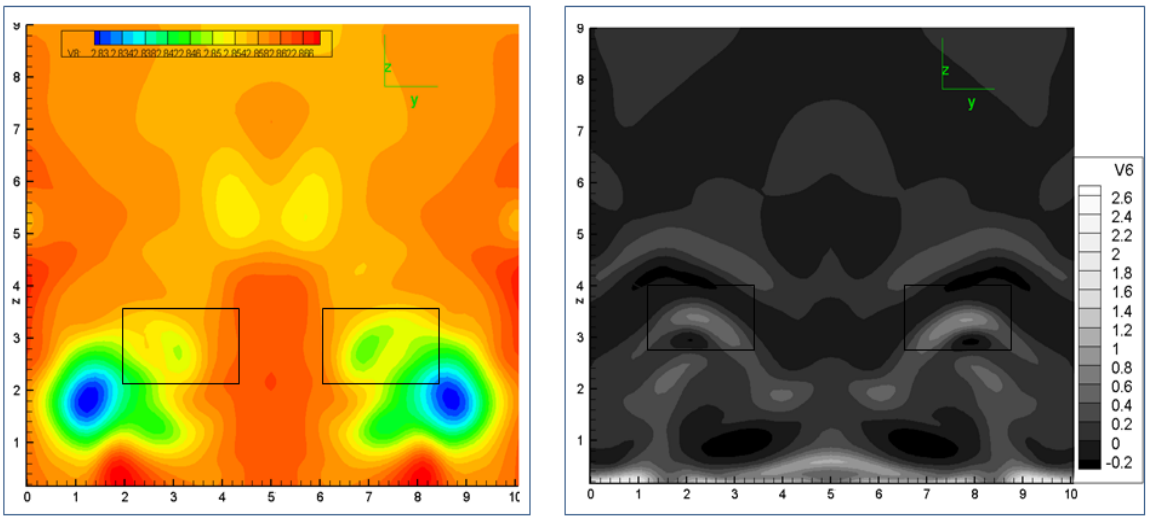

(a) (b)

Figure 4.6: Asymmetric phenomenon started in middle while top and bottom still preserve symmetry($t = 16.75T$); (a) Cross-section of pressure, (b) Cross-section of spanwise vorticity.

view of iso-surface of λ_2 at t=16.25T. From the black rectangles in Figure 4.7, it can be clearly observe that the vortex structures are not symmetric. From here on, we will consider

the above mentioned time step and streamwise location- $t = 16.25T$, $x = 838.9\ \delta_{in}$ - as the origin of such kind of the chaos for our DNS because a significant asymmetric phenomenon starts from that time step and the location. The phenomenon of losing symmetry from the middle ring structure is also reasonable. Since each ring cycle itself is very stable structure, it will be symmetric until it start changing position in spanwise direction.The bottom ring cycle structure is in inviscid zone where it get support from the solid wall so it still keeps symmetry. At the same time the top ring cycle is in inviscid region where the flow is regular so the top will remain symmetric until the sweeps push up the asymmetric small length scales to the top . Hence, the only possible region for originating asymmetric phenomenon is middle ring cycle structure.

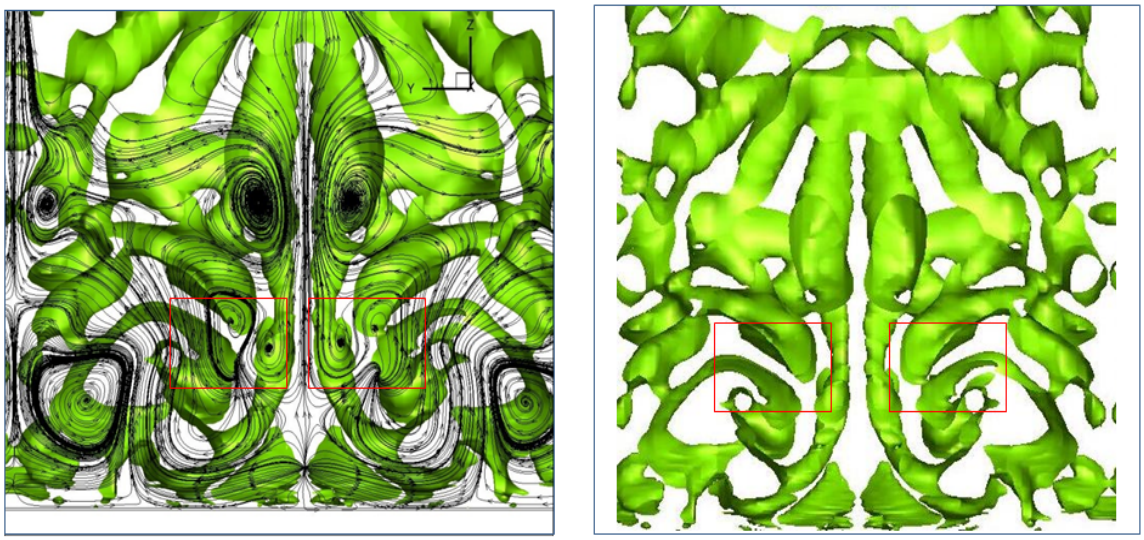

Figure 4.7: 3-D visulization of flow $(t = 16.75T)$; (a) Tail view of iso-surface of λ_2 and stream-trace, (b) Enlarged cross-section of tail view of iso-surface of λ_2.

4.4 Overlapping of multiple-level ring cycles

Figure (4.8) is a side view of iso-surcface of λ_2 at $t = 16.25T$. From this Figure, we observe that the transitional boundary layer is getting thicker and thicker. This thickening is due to overlapping of multiple-level of ring cycles. This overlapping phenomenon can be described in this way. Since, the ring head is located in the inviscid area and has much higher moving speed than the ring legs which are located near the bottom of the boundary layer, the hairpin vortex is stretched and multiple rings are generated. This will lead to an overlapping of second ring cycle upside of the first ring cycle. However, no mixing of two cycles is observed by our new DNS (Figures 10(c) and 9(d)).

The second ring cycle is generated by the wall surface, then separated from wall and

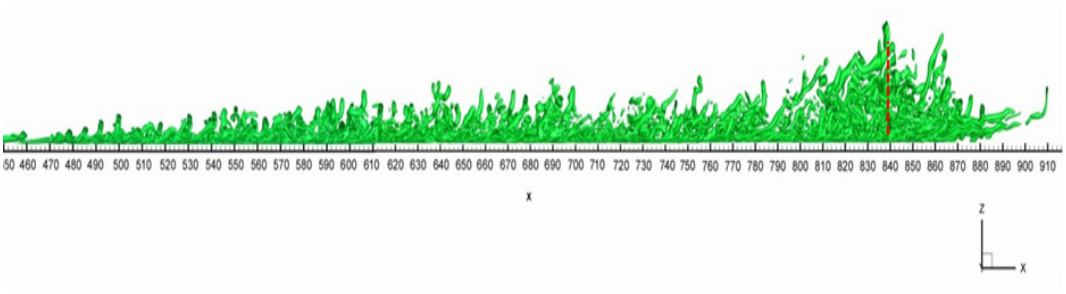

Figure 4.8: Side view of iso-surface of λ_2 for whole domain.

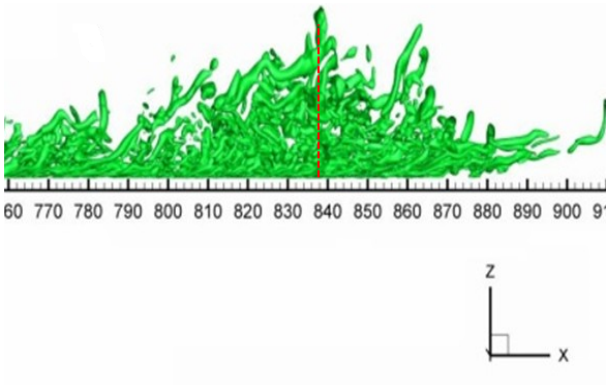

Figure 4.9: Enlarged view side view of iso-surface of λ_2.

convected to downstream. By the same reason the third ring cycle overlaps first two cycles and so on. This is the reason why the transitional boundary layer becomes thicker and thicker.

While investigating the mechanism for flow chaos, it is found an interesting connection between the origin of chaos ($x = 838.9\ \delta_{in}$) and thickness of transitional boundary layer. Figure (4.9), which is enlarged view of Figure (4.8) clearly shows that the asymmetric flow starts from the place where the boundary layer has maximum thickness. More interestingly, it is found that the loss of symmetry begins from nearly the middle of the flow field in the streamwise and spanwise direction. Since, all noises (perturbations) are mainly introduced through the inflow, outflow or far field, it is unlikely that the reason to cause asymmetry is due to the large background noises, but is pretty much the internal property of the multiple-level vortices structures in boundary layer.

4.5 Completely chaotic flow at very late stage

As we found the asymmetric fluctuation is originated at the middle level ring cycle. Another question is immediately raised how this loss of symmetry spreads in the normal direction. To answer this question, we investigate the coherent vertical structures at $t = 17.625T$. By observing Figure 4.10(a), we notice the top level rings still preserve symmetry. Meanwhile we found that the bottom level of ring cycles completely lost symmetry [Figure 4.10 (b)]. This can be concluded that the asymmetric phenomenon which was started in the middle just affected bottom level ring cycle through sweeps. Here we found "Sweeps" motion play important role to spread the asymmetric phenomenon to bottom. Actually, the sweep brings high speed fluid from inviscid region to bottom of boundary layer. The small length scale in bottom is direct consequence of sweeps so these small scales are now victim.

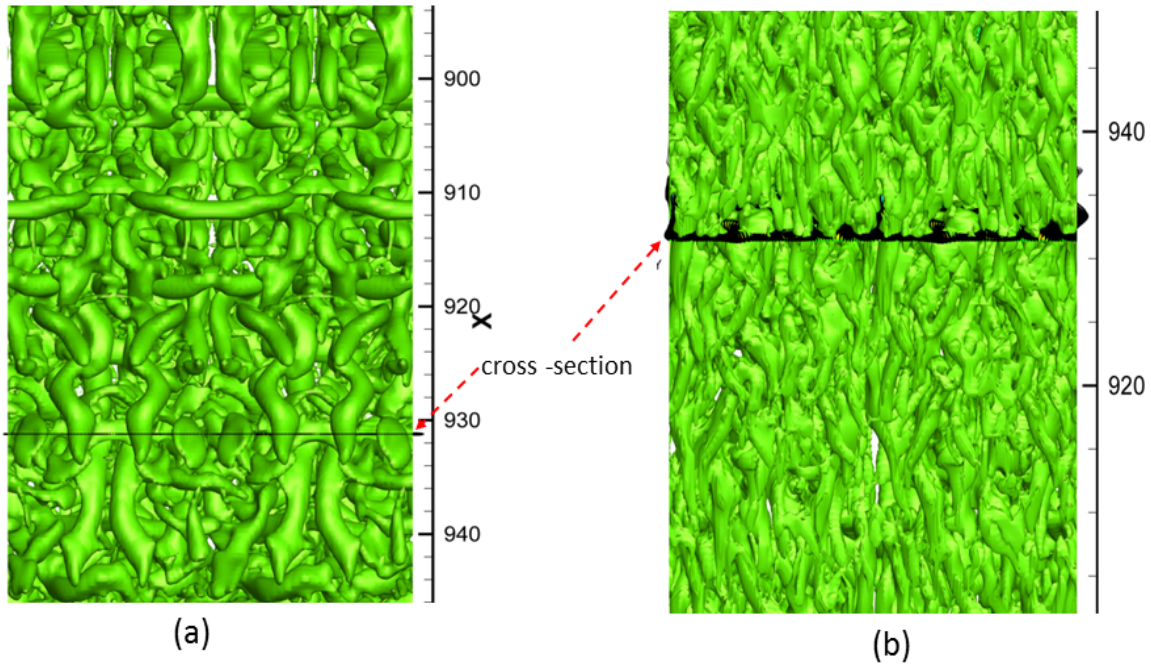

Figure 4.10: Assymetric phenomenon has spreaded to bottom; (a) Top view iso-surface of λ_2, (b) Bottom view iso-surface of λ_2.

To further confirm the claim that the deformed vortices in middle affect the small-scale vortices on bottom, we choose a cross section in Figure 4.10 (a) and (b) at the stream-wise loaction $x \approx 931.5\delta_{in}$. We use stream traces of velocity perturation as shown in Figure 4.12(a). Here, the assymetric fluctation has just spreaded to bottom while top structure is

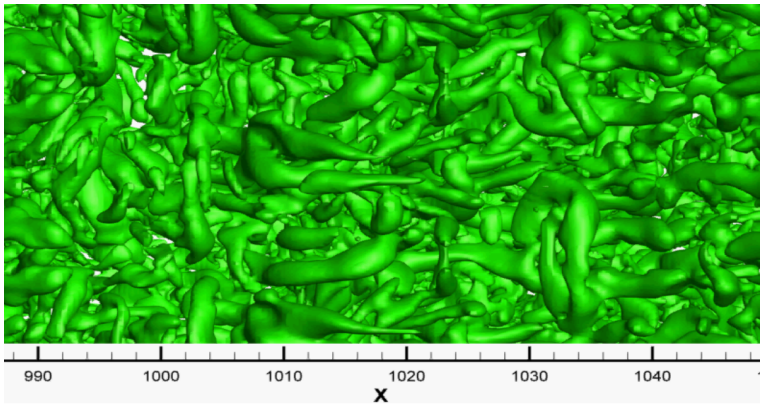

Figure 4.11: Top view of iso-surface of λ_2.

still symmetric. Figure 4.12(b) is one cross-section taken from the Figure (4.11).

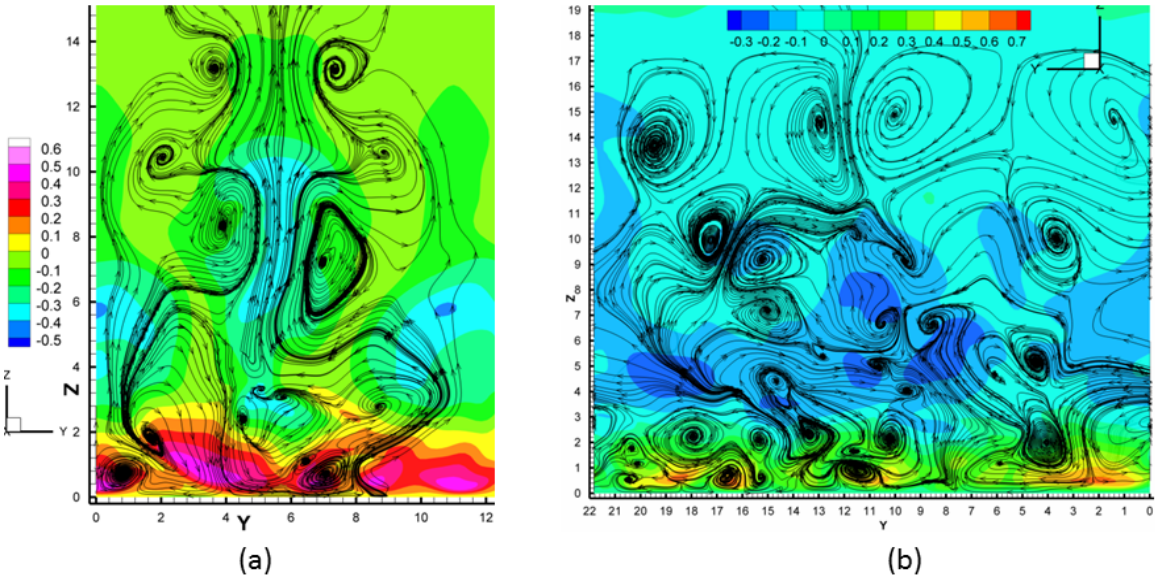

Figure 4.12: Complete chaos at very late stage; (a) Velocity perturbation, (b) Velocity of stream-traces.

4.6 Conclusion

The follwoing conclusions can be made by the current DNS results:

1. The spatial position of the origin of flow chaos for a particular disturbances have been claimed.
2. Although we still use the symmetric boundary condition (period is π for inflow and 2π for the whole domain) without intentional introduction of background noises from the inflow, outflow, and far-field, we still find that the vortices finally become chaos in the whole flow field. Unlike the earlier claim that the origin of the chaos in boundary layer was due to big back ground noises and span-wise periodic boundary condition, we found that the process due to internal property the flow structure and will be triggered by the overlapping of multiple-level ring cycles.

3. There are small vertex rings generated at the middle by different streamwise velocity shear levels which will affect the intensity of positive spikes. This will result in deformation of the small vortices near the bottom of the boundary layer.
4. The asymmetric lower level vortices deform the shape of the upper level vortices through ejection. Simultaneously, the deformed small vortices in middle quickly affect the small length scale in bottom.
5. Finally, we can find that the top flow structure loses the symmetry and the whole flow field is randomized.

CHAPTER 5

SKIN-FRICTION AND BOUNDARY-LAYER THICKENING AT LATE STAGE OF THE TRANSITIONAL FLOW

5.1 Abstract

This part of the dissertation expands upon the results presented in [77] also expends those results by investigating the possible connection with origin of the chaos in late boundary layer transition. The skin-friction drag on a surface of most transportation systems moving in a fluid is one of a prime concern by engineers. It is widely accepted that turbulent flow has higher friction than laminar flow due to the higher mixing in boundary layer. However, our new and well validated high order Direct Numerical Simulation (DNS) data show that the sudden (probably exponential) growth of skin-friction in a laminar-turbulent transitional zone. This can be explained as whenever the small length scales are generated, the velocity shear becomes very large in the laminar sub-layer which is due to momentum increment. Then the surface friction quickly jumps to a very high level even the flow is still transitional phase. Since for incompressible flow the viscous coefficient is a constant, there is no direct co-relation between high surface friction and turbulence mixing. Therefore, high skin-friction is only directly related to velocity gradient which is immediately provoked by small length scale generation near the wall. From the earlier experiments it is found that the turbulent boundary layer is much thicker than laminar boundary layer. This part also presents the mechanism that why the overlapping of multiple-level ring cycles play an important role for the boundary layer thickening in transitional flow. Numerical data obtained from our DNS shows that the second and third level of multiple ring cycles would overlap with the primary level of multiple ring cycle since ring head usually located

in inviscid region will have greater velocity than ring legs attached in bottom(viscid region). Another interesting phenomena is that even the second ring cycle directly over lap first and also have sign of viscosity but still does not mix with the first ring cycle. Actually these ring cycles are separated by a secondary vortex rings which are generated by the wall surface and moved to the middle between two ring cycles. The overlapping of multiple ring cycles leads to thickening of the transitional boundary layer.

5.2 Background and motivation

As aviation and marine industries are growing bigger and bigger, the fuel consumption and emission of harmful gases on air being an important issue. Engineers are always concerned for designing energy-efficient and environmentally appropriate technologies. While talking about fuel economy in aircraft and ship, one of the main interest lies in the skin-friction drag reduction in boundary surface since it is a main contributor to the total drag and can contribute up to 50% for a subsonic transport aircraft [78] and upto 60% of a ship's total resistance when Froude number is on the order of 10^{-1} [79]. Skin-friction is also an important factor for depicting the turbulent state of flow in boundary layer, which is important both to basic understanding of such kind of flows and to assist in boundary layer control. As a result, there has been numerous amount of experimental and numerical research work related to the skin-friction drag, specially how to reduce the shear-stress in wetted surface and many novel technologies such as boundary layer delay, aircraft surface laminarization, boundary layer suction and surface cooling etc. have been implemented. Mainly, two types of methods have used to reduce the skin-friction such as active (e.g. gas or polymer injection) and passive (e.g. hydrophobic coating) methods [4, 80].

For the recent years the interest for the laminar flow control (LFC) has increased greatly [81]. Laminar flow control is an active boundary-layer flow control technique,

which will be beneficial to maintain the laminar flow (LF) state at chord Reynolds numbers behind those that are normally considered to be transitional or turbulent state with out use of control [82]. It is important to note that the laminar flow control doesn't imply the relaminarization of a turbulent flow. It has been shown experimentally that the surface friction coefficient for the turbulent boundary layer may be two to five times greater than that laminar layer at same Reynolds number [83]. Obviously, laminar flow will be more desirable than the turbulent one from the view point of skin-friction drag reduction of aircraft. Although achieving the laminar over an entire domain is impractical due to sensitivity of laminar flow with external disturbances,the drag reduction generated by LF over selected portions of a vehicle (for example, for an aircraft,the wing, engine nacelles, fuselage nose etc are candidates for achieving LF) is achievable.

Meanwhile, some of the current researches also have been focusing on how to design a device that can artificially increase the thickness of the boundary layer in the wind tunnel. For instances, one way to increase is by using an array of varying diameter cross flow jets with the jet diameter reducing with distance downstream and there are other methods like boundary layer fence, array of cylinders, gauze screen, or distributed drag method [84].

It is well-known that turbulent boundary-layers are much thicker than the laminar layer. However, there are few literature related for the mechanism of the multi-level rings overlapping and how boundary-layer thickening. From the Figure (5.1) which is taken from the book of Schilichting, it can be clearly noted that the boundary layer becomes thicker and thicker while the flow state is changing from laminar to turbulence. This phenomenon is also observed by our DNS of flow transition over a flat plate. Figure (5.2) is visualization of the multiple-level ring overlapping. Moreover, even though they have same direction of rotation still never mix to each other.

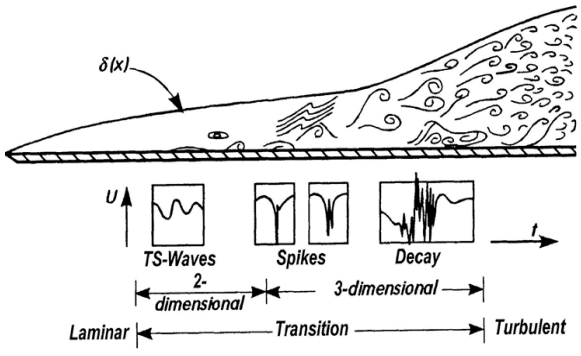

Figure 5.1: Schematic of flow transition on a flat plate(page 474,Boundary-Layer Theory by Schilichting et al, (2000)[26])

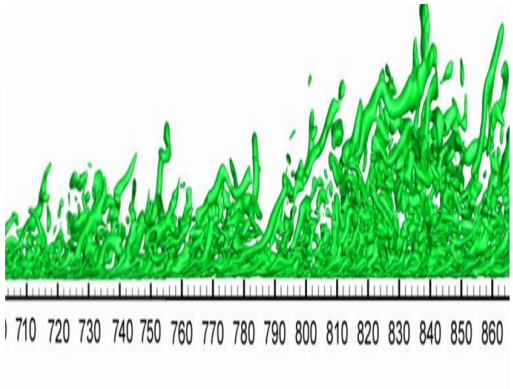

Figure 5.2: Mutliple ring cycles overlapping and boundary thickening (our DNS)

5.3 Relation between small length-scale vortices generation and skin-friction coefficient

The concept of " hairpin vortex breakdown" was well accepted and it was further assumed that the process of breakdown was responsible for small scale generation (turbulence formation) [26, 85]. However, from our DNS results, we didn't observe any " breakdown" [Figure 5.5] moreover it is impossible theoretically [11] as well. The immediate question is how the small-scale vortices are generated. Interestingly, all small vortices, and thus turbulence, are generated by high shear (HS) layer near the wall instead of by "vortex breakdown" [5]. From the Figure (5.3) and (5.4) it can be easily observe that lots of small-length scales are already generated around HS and most of them appear between

the bottom of the wall and the high shear layer region and some of them are located above the HS.

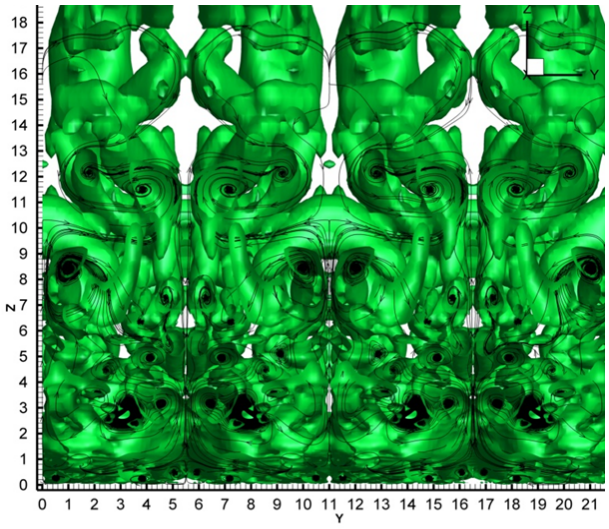

Figure 5.3: 3-D visualization of flow with stream traces at $t = 15.0T$ and $x = 508.633\delta_{in}$ [Ping Lu et al., (2011)]

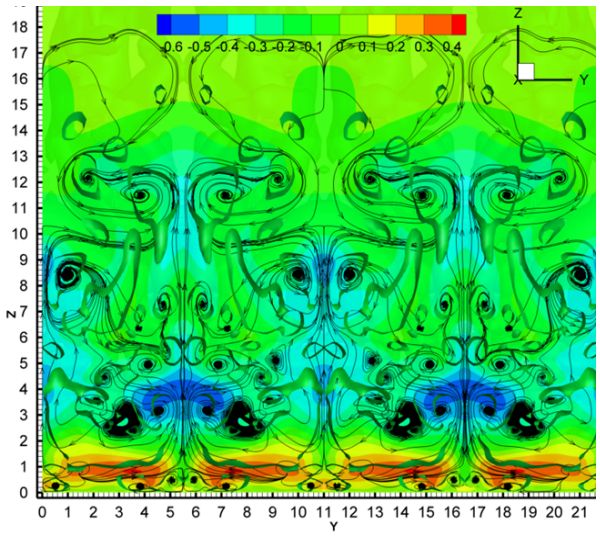

Figure 5.4: 3-D visualization of flow with stream traces and velocity perturbation at $t = 15.0T$ and $x = 508.633\delta_{in}$ [Ping Lu et al., (2011)]

Figure (5.5) is the 3-D visualization of late stage of transition by bottom view. Meanwhile, the shapes of positive spikes along x-direction is shown in Figure (5.6). Actually, these positive spikes are formed due to the sweep motion of inviscid fluid. Originally, these spikes are formed separately with different intensity later combine together to form a much stronger high speed area. Finally, two red regions (high speed areas) depart further under the ring-like vortex.

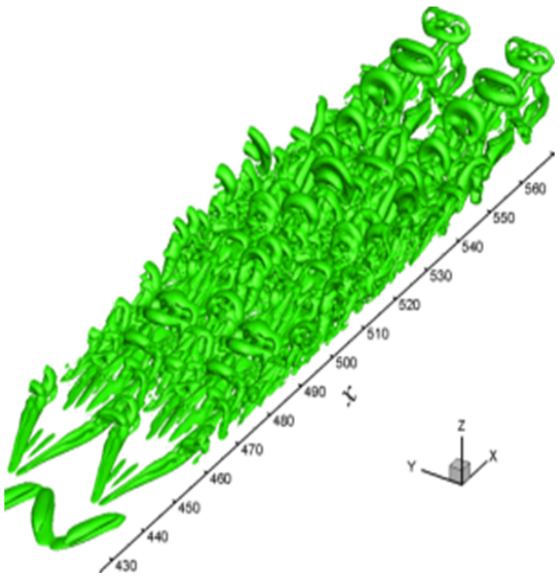

Figure 5.5: Visualization of flow transition at $t = 18.0T$ based on eigenvalue λ_2.

To investigate the relation between small length scale vortices generation and sudden increment of skin- friction, we will first analyze one of two slices from Figure 5.7(a) in more details. The streamwise location of the positive spikes and their wall-normal positions with the co-existing small structures can be observed in this section. Figure 5.7(a) demonstrates that the small length scales (turbulence) are generated near the wall surface in the normal direction and Figure 5.7(b) is the contour of velocity perturbation at an enlarged section $x = 508.63$ in the streamwise direction. Red spots at the Figure 5.7(b) indicates

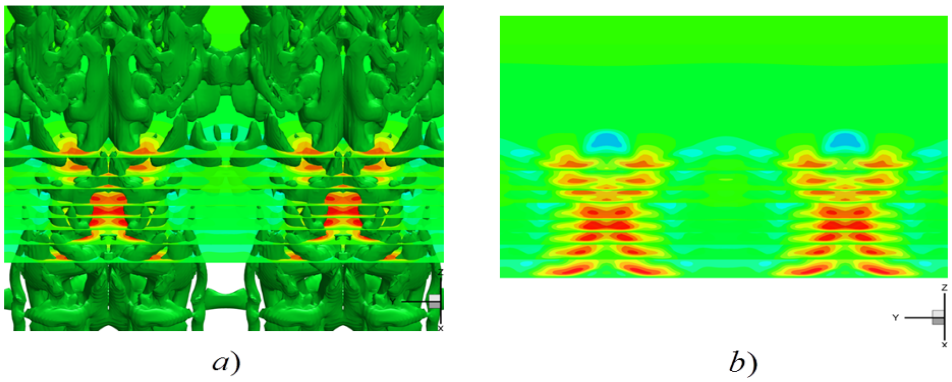

Figure 5.6: (a) bottom view of λ_2 structure;(b)Visualization of shape of positive spikes along x-direction.

the region of high shear layer generated around the spike. It shows that small vortices are all generated around the high speed region (positive spikes) due to instability of high shear layer, especially the one between the positive spikes and solid wall surface.

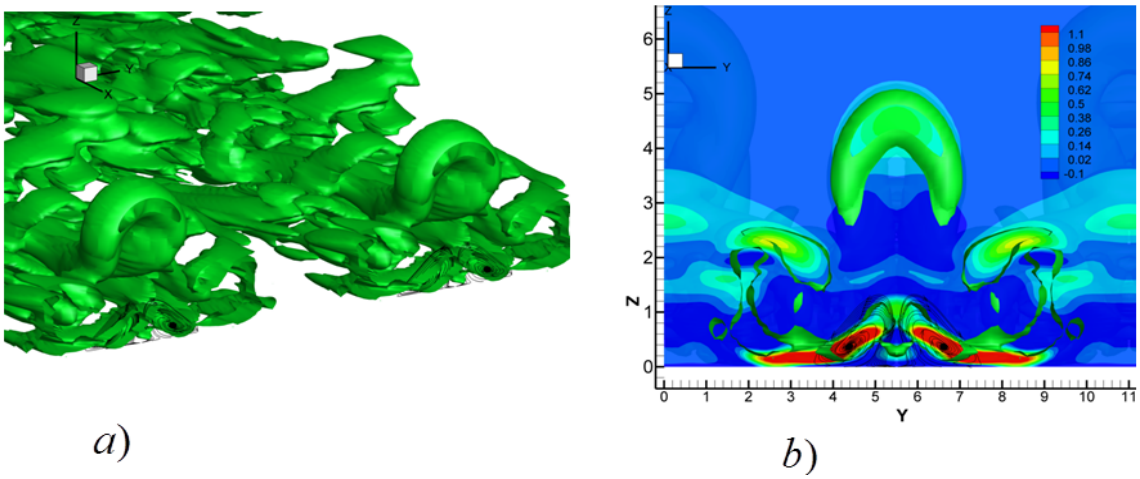

Figure 5.7: (a) Isosurface of λ_2 and streamtrace at $x = 508.633\delta_{in}$; (b) Iso-surface of λ_2 and velocity perturbation at x=508.633 δ_{in}.

Figure (5.8) is a graph plotted the skin-friction coefficient calculated from the time-averaged and spanwise-averaged profile along various streamwise locations. The spatial evolution of skin-friction coefficients of laminar flow is also plotted out for comparison.

It is observed from this figure that the sharp growth of the skin-friction coefficient occurs after $x \approx 450\delta_{in}$, which is defined as the "onset point". The skin-friction coefficient after transition is in good agreement with the flat-plate theory of turbulent boundary layer by Cousteix in 1989 [62].

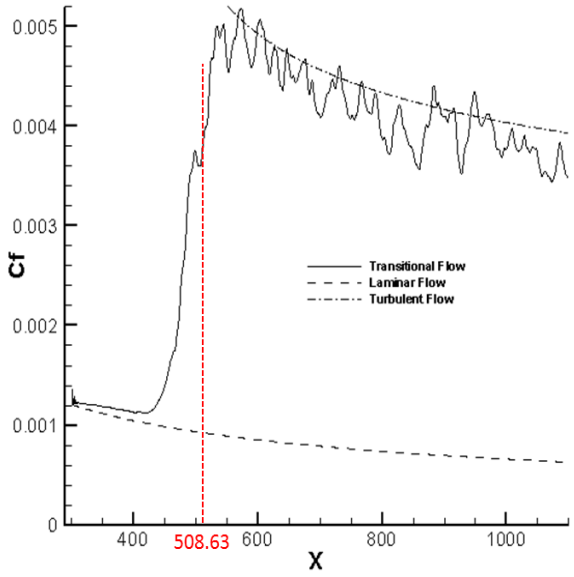

Figure 5.8: Streamwise evolutions of the time and spanwise averaged skin-friction coefficient.

To collect more supporting materials for the relationship between the downdraft motions and small length scale vortex generation we take consider the four ring-like vortices at different spanwise locations and for same time step $t = 8.0T$ as shown in Figure (5.9). When the primary vortex ring is perpendicular and perfectly circular, it will generate a strong second sweep which brings a lot of energy from the inviscid area to the bottom of the boundary layer and makes that area very active. However, when the heading primary ring is skewed and sloped but no longer perfectly circular and perpendicular, the second sweep immediately becomes weak. This phenomenon can be verified from Figure (5.10)

that the sweep motion is getting weak as long as the vortex rings do not keep perfectly circular and perpendicular.

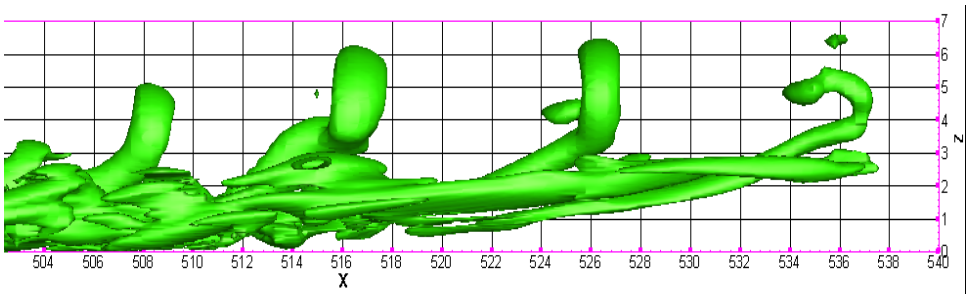

Figure 5.9: Side view for multiple-level ring cycles at $t = 8.0T$.

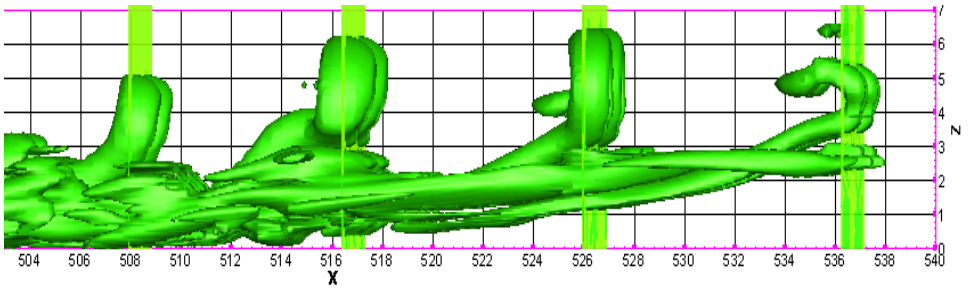

Figure 5.10: Side view for multiple rings with vector distribution at $t = 8.0T$.

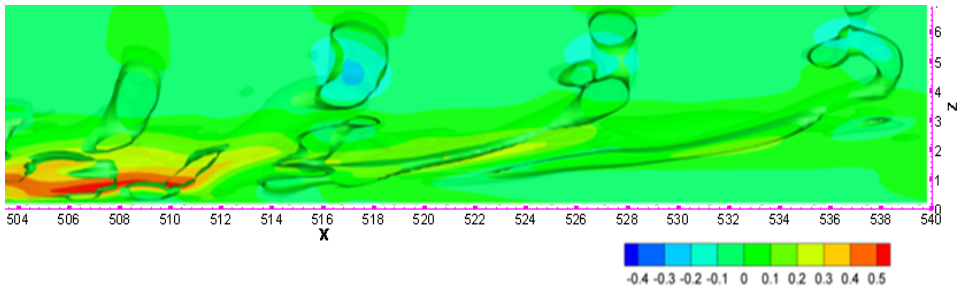

Figure 5.11: Side view for multiple rings with velocity perturbation at $t = 8.0T$.

By looking at Figure 5.11 around the region of $x = 508\delta_{in}$, we note that there is a high speed area (red color region) under the ring-like vortex, which is caused by the strong sweep motion. However, for the ring located at $x = 537\delta_{in}$, we can see there is no high speed region below the first ring due to the weakness of the sweep motion. That gives us an idea that we can try to change the gesture and shape of the vortex rings in order to reduce the intensity of positive spikes. Eventually, the skin friction can be reduced consequently.

5.4 Conclusion

At the late stage of transition, the flow is essentially nonlinear and complex so it's very hard to approach. However, based on our recent numerical simulation, the following conclusions can be made.

1. There is direct relationship between The enlargement of skin-friction and the small length scale vortices generation during the transition process. It clearly indicates that the shear stress is only related to velocity gradient rather than viscosity change.
2. If the ring-like vortex is skewed and/or the standing position is inclined,the second sweep from the vortex and the intensity of the positive spikes will be weakened. This direct consequence is that small length scales quickly damp. This might be an important indication that we should mainly consider the sharp velocity gradients for turbulence modeling instead of only considering the change of viscous coefficients in the near wall region.
3. The overlapping of multiple-level ring cycles is the main region for the thickening of the transitional boundary layer. However, they never mix because the two different level cycles are separated by a vortex trees which has a different sign with the primary vortex cycle.

APPENDIX A

MORE VISUALIZATION ABOUT LATE STAGE OF FLOW

A.1 Nature of flow field at the late stage of transition

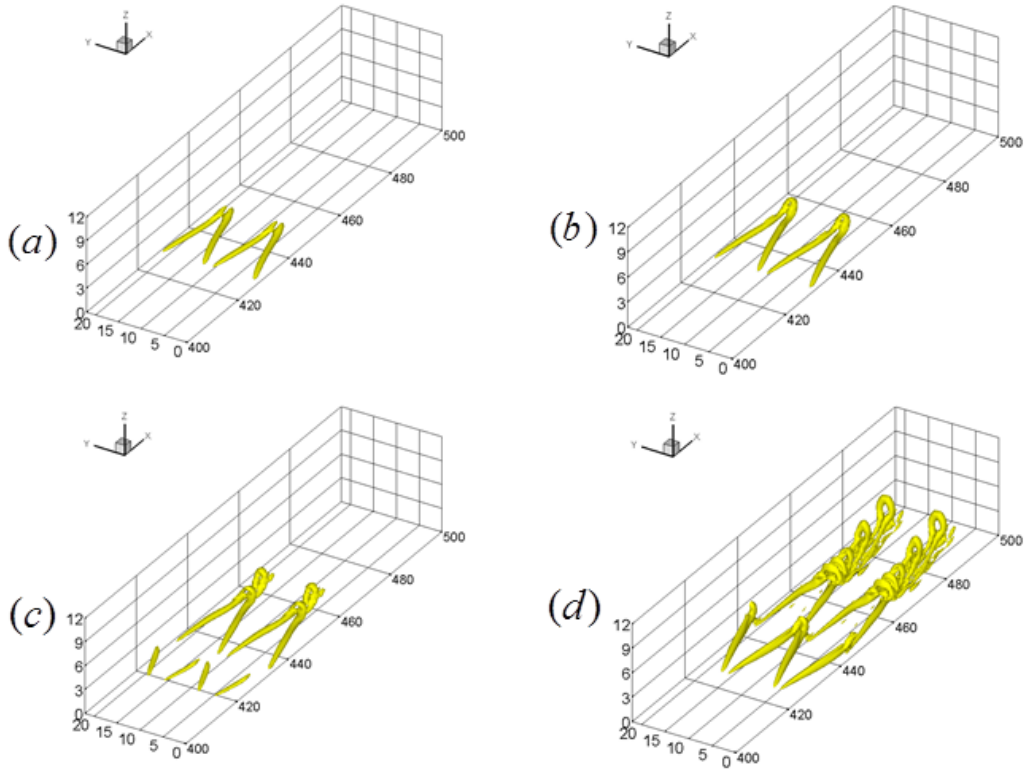

Figure A.1: Ring type vortex generation, $\lambda_2 = -0.001$; (a) t=6.0T, (b) t=6.2T, (c) t=6.4T, (d) t=7.0T

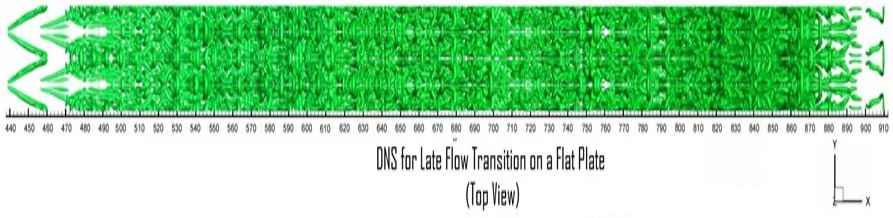

Figure A.2: 3-D visualization of flow field , $\lambda_2 = -0.001$; t=16.25T

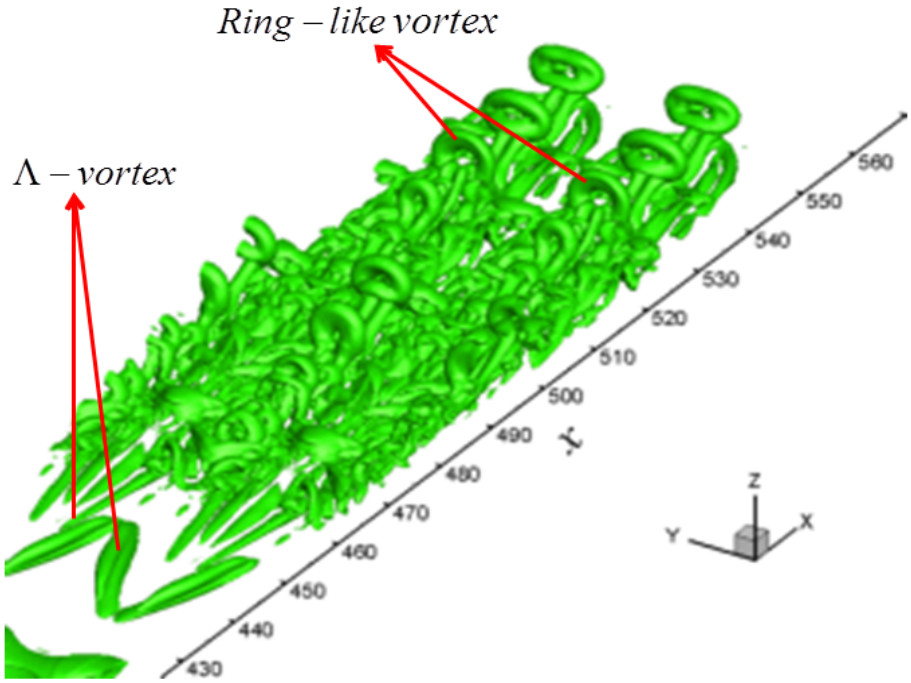

Figure A.3: Visualization of coherent structures at late of flow , $\lambda_2 = -0.001; t = 8.2T$,

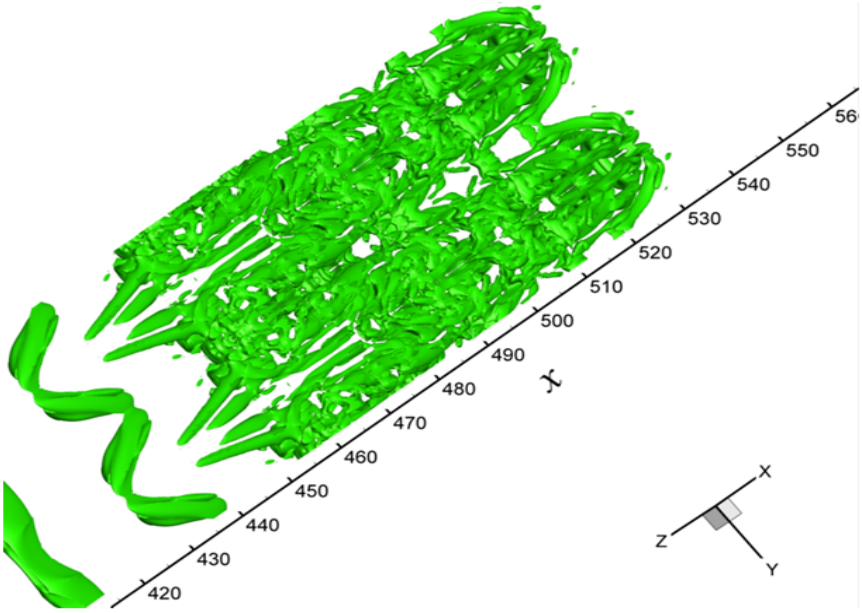

Figure A.4: Back view of coherent structures at $\lambda_2 = -0.001; t = 8.0T$,

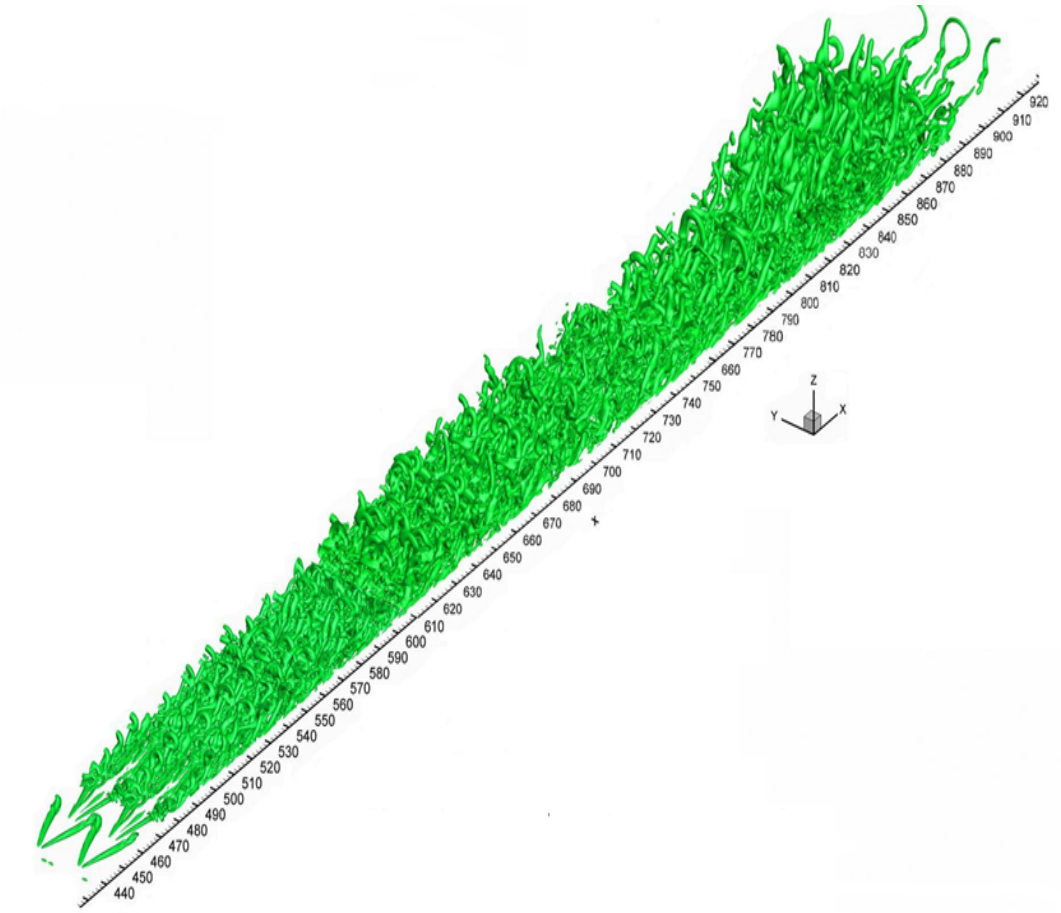

Figure A.5: Complete flow visualization at late transition for $\lambda_2 = -0.001; t = 16.25T$,

REFERENCES

[1] I. Tani. Boundary-layer transition. *Annual Review of Fluid Mechanics*, 1(1):169–196, 1969.

[2] Y. S. Kachnaov. Physical mechanisms of laminar-boundary-layer transition. *Annu. Rev.Fluid Mech.*, 26:411–482, 1994.

[3] W. S. Saric, H. L. Reed, and E. J. Kerschen. Boundary-layer receptivity to freestream disturbances. *Annual review of fluid mechanics*, 34(1):291–319, 2002.

[4] E. Coustols and A. M. Savill. Turbulent skin-friction drag reduction by active and passive means. part 1. everything you wanted to know about riblets, lebus and other devices. Technical report, DTIC Document, 1992.

[5] P. Lu and C. Liu. Dns study on mechanism of small length scale generation in late boundary layer transition. *Physica D: Nonlinear Phenomena*, 241:11–24, 2011.

[6] P. Lu, M. Thapa, and C. Liu. Numerical study on randomization in late boundary layer transition. 2012.

[7] D. G. W. Meyer, U. Rist, and Kloker M. J. Investigation of the flow randomization process in a transitional boundary layer. In: Krause, E.; Jger, W. (eds.). In *High Performance Computing in Science and Engineering 03. Transactions of the HLRS 2003*, pages 239–253. Springer, 2003.

[8] U. Frisch. Turbulence. *Turbulence, by Uriel Frisch, pp. 310. ISBN 0521457130. Cambridge, UK: Cambridge University Press, January 1996.*, 1, 1996.

[9] P. A. Davidson. *Turbulence: An Introduction for Scientists and Engineers: An Introduction for Scientists and Engineers*. Oxford University Press, 2004.

[10] A. Tsinober. *An informal introduction to turbulence*, volume 63. Springer, 2001.

[11] C. Liu. Numerical and theoretical study on vortex breakdown. *International Journal of Computer Mathematics*, 88(17):3702–3708, 2011.

[12] T. Cebeci. *Analysis of turbulent boundary layers*. Academic Press, 1974.

[13] J. Mathieu and J. Scott. *An introduction to turbulent flow*, volume 1. Taylor & Francis, 2000.

[14] C. Liu, L. Chen, and P. Lu. New findings by high-order dns for late flow transition in a boundary layer. *Modelling and Simulation in Engineering*, 2011:1, 2011.

[15] C. Liu and L. Chen. Parallel dns for vortex structure of late stages of flow transition. *Computers & Fluids*, 45(1):129–137, 2011.

[16] L. F. Richardson and S. Chapman. *Weather prediction by numerical process*. Dover publications New York, 1965.

[17] A. N. Kolmogorov. The local structure of turbulence in incompressible viscous fluid for very large reynolds numbers. In *Dokl. Akad. Nauk SSSR*, volume 30, pages 299–303, 1941.

[18] A. N. Kolmogorov. The local structure of turbulence in incompressible viscous fluid for very large reynolds numbers. *Proceedings of the Royal Society of London. Series A: Mathematical and Physical Sciences*, 434(1890):9–13, 1991.

[19] U. Frisch. Turbulence: the legacy of a. n. kolmogorov, 1995.

[20] C. Segal and T. L. Carus. *Lucretius on death and anxiety: poetry and philosophy in De rerum natura*. Princeton University Press Princeton, NJ, 1990.

[21] O. Darrigol. *Worlds of flow: A history of hydrodynamics from the Bernoullis to Prandtl*. Oxford University Press, 2005.

[22] W. Tollmien. Über die entstehung der turbulenz. 1. mitteilung. *Nachrichten von der Gesellschaft der Wissenschaften zu Göttingen, Mathematisch-Physikalische Klasse*, 1929:21–44, 1928.

[23] H. Schlichting. Zur enstehung der turbulenz bei der plattenströmung. *Nachrichten von der Gesellschaft der Wissenschaften zu Göttingen, Mathematisch-Physikalische Klasse*, 1933:181–208, 1933.

[24] K. S. Gage and W. H. Reid. The stability of thermally stratified plane poiseuille flow. *J. Fluid Mech*, 33(1):21–32, 1968.

[25] G. B. Schubauer and H. K. Skramstad. Laminar-boundary-layer oscillations and transition on a flat plate, 1948.

[26] H. Schlichting and K. Gersten. *Boundary-layer theory*. Springer, 2000.

[27] J. Laufer and T. Vrebalovich. Stability and transition of a supersonic laminar boundary layer on an insulated flat plate. *J. Fluid Mech*, 9(pt 2):257–299, 1960.

[28] C. J. Allen and J. W. Kendall. Maturation of the circadian rhythm of plasma corticosterone in the rat. *Endocrinology*, 80(5):926–930, 1967.

[29] F. M. White. *Viscous Fluid Flow third edition*. Tata McGraw-Hill Education, 1974.

[30] E. Reshotko. Boundary-layer stability and transition. *Annual Review of Fluid Mechanics*, 8(1):311–349, 1976.

[31] T. Herbert. Secondary instability of boundary layer. *Annu. Rev.Fluid Mech.*, 20:487–526, 1988.

[32] M. V. Morkovin. On the many faces of transition. *Viscous Drag Reduction*, pages 1–31, 1969.

[33] M. V. Morkovin and E. Reshotko. Dialogue on progress and issues in stability and transition research. In *Laminar-turbulent transition*, pages 3–29. Springer, 1990.

[34] M. V. Morkovin. Bypass transition to turbulence and research desiderata. In *In NASA. Lewis Research Center Transition in Turbines*, volume 1, pages 161–204, 1985.

[35] E. Reshotko. Environment and receptivity. In *In AGARD Spec. Course on Stability and Transition of Laminar Flow 11 p (SEE N84-33757 23-34)*, volume 1, 1984.

[36] L. M. Mack. *Boundary-layer stability theory*. Jet Propulsion Laboratory, 1969.

[37] L. Chen and C. Liu. Numerical study on mechanisms of second sweep and positive spikes in transitional flow on a flat plate. *Journal of Computers and Fluids*, 40:28–41, 2011.

[38] P. S. Klebanoff, K. D. Tidstrom, and L. M. Sargent. The three-dimensional nature of boundary-layer instability. *J. Fluid Mech*, 12(1):1–34, 1962.

[39] S. Bake, Y. S. Kachanov, and H. H. Fernholz. Subharmonic k-regime of boundary-layer breakdown. *Transitional boundary layers in aeronautics*, pages 81–88, 1996.

[40] S. Bake, H. H. Fernholz, and Y. S. Kachanov. Resemblance of k-and n-regimes of boundary-layer transition at late stages. *European Journal of Mechanics-B/Fluids*, 19(1):1–22, 2000.

[41] V. I. Borodulin, V. R. Gaponenko, and Y. S. Kachanov. Generation and development of coherent structures in boundary layer at pulse excitation. In *Xth International Conference on Methods of Aerophysical Research. Proceedings. Part II*, pages 37–42. DTIC Document, 2000.

[42] L. Kleiser and T. A. Zang. Numerical simulation of transition in wall-bounded shear flows. *Annu. Rev.Fluid Mech.*, 23:495–537, 1991.

[43] N. D. Sandham and L. Kleiser. The late stages of transition to turbulence in channel flow. *Journal of Fluid Mechanics*, 245(1):319–348, 1992.

[44] U. Rist and H. Fasel. Direct numerical simulation of controlled transition in a flat-plate boundary layer. *Journal of Fluid Mechanics*, 298:211–248, 1995.

[45] V. I. Boroduln, V. R. Gaponenko, and Y. S. Kachanov. Late-stage transition boundary-layer structure: direct numerical simulation and exerperiment. *Theoret.Comput.Fluid Dynamics*, 2002.

[46] S. Bake, D. Meyer, and U. Rist. Turbulence mechanism in klebanoff transition:a quantitative comparison of experiment and direct numerial simulation. *J. Fluid Mech.*, 459:217–243, 2002.

[47] Y. S. Kachanov. On a universal mechanism of turbulence production in wall shear flows. in: Notes on numerical fluid mechanics and multidisciplinary design. In *Recent Results in Laminar-Turbulent Transition*, volume 86, pages 1–12. Springer, 2003.

[48] R. J. Adrian. Hairpin vortex organization in wall turbulence. *Physics of Fluids*, 19, 2007.

[49] X. Wu and P. Moin. Direct numerical simulation of turbulence in a nominally zero-pressure gradient flat-plate boundary layer, jfm, vol 630, pp5-41, 2009. *J. Fluid Mech.*, 630:5–41, 2009.

[50] H. Guo, V. I. Borodulin, Y. S. Kachanov, C. Pan, J. J. Wang, X. Q. Lian, and S. F. Wang. Nature of sweep and ejection events in transitional and turbulent boundary layers. *J of Turbulence*, 2010.

[51] L. Jiang, H. Shan, and C. Liu. Direct numerical simulation of boundary-layer receptivity for subsonic flow around airfoil. In *Recent Advances in DNS and LES*, pages 203–218. Springer, 1999.

[52] C. Liu, Z. Liu, and S. McCormick. Multigrid methods for flow transition in a planar channel. *Computer Physics Communications*, 65(1):188–200, 1991.

[53] C. Liu and Z. Liu. Multigrid mapping and box relaxation for simulation of the whole process of flow transition in 3d boundary layers. *Journal of Computational Physics*, 119(2):325–341, 1995.

[54] Z. Liu, C. Liu, and G. Xiong. A contravariant velocity based implicit multilevel method for simulating the whole process of incompressible flow transition arround joukowsky airfoils. *Applied Mechanics and Engineering*, 3:111–161, 1998.

[55] S. K. Lele. Compact finite difference schemes with spectral-like resolution. *Journal of Computational Physics*, 103(1):16–42, 1992.

[56] C. W. Shu and S. Osher. Efficient implementation of essentially non-oscillatory shock-capturing schemes. *Journal of Computational Physics*, 77(2):439–471, 1988.

[57] L. Jiang, H. Shan, C. Liu, and M. R. Visbal. Non-reflecting boundary conditions for dns in curvilinear coordinates. In *Recent Advances in DNS and LES*, pages 219–233. Springer, 1999.

[58] M. R. Malik. Numerical methods for hypersonic boundary layer stability. *Journal of Computational Physics*, 86(2):376–413, 1990.

[59] L. Jiang, C. L. Chang, M. Choudhari, and C. Liu. Cross-validation of dns and pse results for instability wave propagation in compressible boundary layers past curvilinear surfaces. *AIAA paper*, 3555, 2003.

[60] H. Shan, L. Jiang, and C. Liu. Direct numerical simulation of flow separation around a naca 0012 airfoil. *Computers & fluids*, 34(9):1096–1114, 2005.

[61] L. M. Mack. Boundary-layer linear stability theory. Technical report, DTIC Document, 1984.

[62] F. Duros, P. Comte, and M. Lesieur. Large eddy simulation of transition to turbulence in a boundary layer developing spatially over a flat plate. *J. Fluid Mech.*, 326:1–36, 1996.

[63] L. Prandtl. Über flüssigkeitsbewegung bei sehr kleiner reibung. *Int. Math. Kongr Heidelberg. Leipzig*, 1904.

[64] J. D. Anderson Jr. Ludwig prandtls boundary layer. *Physics Today*, 58(12):42–48, 2005.

[65] C. R. Illingworth. Unsteady laminar flow of gas near an infinite flat plate. In *Mathematical Proceedings of the Cambridge Philosophical Society*, volume 46, pages 603–613. Cambridge Univ Press, 1950.

[66] E. R. Van Driest. *Investigation of laminar boundary layer in compressible fluids using the Crocco method*. National Advisory Committee for Aeronautics, 1952.

[67] M. R. Head and P. Bandyopadhyay. New aspects of turbulent boundary-layer structure. *J. Fluid Mech*, 107:297–338, 1981.

[68] B. J. Cantwell. Organized motion in turbulent flow. *Annual Review of Fluid Mechanics*, 13(1):457–515, 1981.

[69] P. Moin and J. Kim. Numerical investigation of turbulent channel flow. *Journal of fluid mechanics*, 118:341–377, 1982.

[70] M. Thapa, P. Lu, and C. Liu. Dns study for the origin of the chaos in late boundary layer transition. *Global Journal of Mathematical Sciences (GJMS)*, 2(1), 2013.

[71] J. Jeong and F. Hussain. On the identification of a vortex, j. fluid mech. *Annu. Rev.Fluid Mech.*, 285:69–94, 1995.

[72] L. Chen, D. Tang, P. Lu, and C. Liu. Evolution of the vortex structures and turbulent spots at the late-stage of transitional boundary layers. *Science China, Physics, Mechanics and Astronomy*, 53:1–14, 2010.

[73] E. R. Corino and R. S. Brodkey. A visual investigation of the wall region in turbulent flow. *Journal of Fluid Mechanics*, 37(01):1–30, 1969.

[74] W. W. Willmarth and S. S. Lu. Structure of the reynolds stress near the wall. *J. Fluid Mech*, 55(1):65–92, 1972.

[75] L. Chen, X. Liu, M. Oliveira, and C. Liu. Dns for ring-like vortices formation and roles in positive spikes formation. *AIAA Paper 2010-1471*, 2010.

[76] C. Liu and L. Chen. Study of mechanism of ring-like vortex formation in late flow transition. *AIAA Paper 2010-1456*, 2010.

[77] P. Lu, M. Thapa, and C. Liu. Numerical study on surface friction and boundary layer thickening in transitional flow.

[78] J. J. Thibert, J. Reneaux, and V. Schmitt. Onera activities on drag reduction. *Tiré à part- Office national d'études et de recherches aerospatiales*, 1990.

[79] B. R. Elbing, D. R. Dowling, M. Perlin, and S. L. Ceccio. Diffusion of drag-reducing polymer solutions within a rough-walled turbulent boundary layer. *Physics of Fluids*, 22:045102, 2010.

[80] T. Min and J. Kim. Effects of hydrophobic surface on skin-friction drag. *Physics of Fluids*, 16:L55, 2004.

[81] H. Bieler, A. Abbas, J. Y. Chiaramonte, and D. Sawyers. Flow control for aircraft performance enhancementsoverview of airbusuniversity cooperation. *AIAA Paper*, 3692:2006, 2006.

[82] R. D. Joslin. Aircraft laminar flow control 1. *Annual review of fluid mechanics*, 30(1):1–29, 1998.

[83] O. A. Gross. Skin friction and stability of a laminar binary boundary layer on a flat plate. 1963.

[84] J. E. Sargison, G. J. Walker, V. Bond, and G. Chevalier. Experimental review of devices to artificially thicken wind tunnel boundary layers. 2004.

[85] B. A. Singer and R. D. Joslin. Metamorphosis of a hairpin vortex into a young turbulent spot. *Physics of Fluids*, 6:3724, 1994.

BIOGRAPHICAL STATEMENT

Manoj K. Thapa was born in Nepal in 1980. He received his B.S. and Master degrees from Tribhuvan University, Nepal, in 2003 and 2005 respectively. He came to United States of America in 2009 Fall and completed his Ph.D. degree in Computational Fluid Dynamics from The University of Texas at Arlington in December, 2013. His main area of research interests are numerical analysis and fluid dynamics. He is a student member of American Institute of Aeronautics and Astronautics (AIAA).